

Using Piecewise Potential Vorticity Inversion to Diagnose Frontogenesis. Part I: A Partitioning of the \mathbf{Q} Vector Applied to Diagnosing Surface Frontogenesis and Vertical Motion

MICHAEL C. MORGAN

Department of Atmospheric and Oceanic Sciences, University of Wisconsin—Madison, Madison, Wisconsin

(Manuscript received 3 August 1998, in final form 11 November 1998)

ABSTRACT

The technique of piecewise potential vorticity (PV) inversion is used to identify the nondivergent wind fields attributed to upper-, middle-, and lower-tropospheric PV anomalies in addition to the irrotational wind with the goal of diagnosing the respective wind fields' frontogenetic potentialities. Frontogenesis is diagnosed using a piecewise separation of the \mathbf{Q} vector into parts associated with the partitioned wind field. Partitioned geostrophic \mathbf{Q} vectors are used to diagnose the vertical motion attributed to the upper-, middle-, and lower-tropospheric PV anomalies.

Insight gained from this new diagnostic technique is demonstrated by examining a particular case of extratropical marine cyclogenesis resulting from the interaction of an upper-tropospheric short-wave trough with a surface thermal wave. In the early stages of development, the largest contributor to surface frontogenesis was associated with winds attributed to the lower-tropospheric thermal wave. As the cyclone matured, the contributions of the upper-tropospheric PV and near-surface potential temperature anomalies to surface frontogenesis increased. Winds attributed to the upper-tropospheric PV were frontogenetical north of the thermal ridge axis and frontolytical south of the thermal ridge in the warm sector. The upper-tropospheric PV acted to amplify the thermal ridge while simultaneously narrowing the warm sector. The patterns of geostrophic \mathbf{Q} vectors associated with the upper-tropospheric PV suggest that ascent should be favored in the narrowing surface thermal ridge. The contribution to surface frontogenesis due to lower- and middle-tropospheric PV, whose increase is imputed to latent heat release, was variable during the evolution of the cyclone—suggesting that the location of diabatically generated PV anomalies relative to frontal zones can have a significant impact on frontogenesis and associated frontal precipitation distribution. Throughout the evolution of the cyclone, the irrotational wind was frontogenetical along the warm and cold fronts with the magnitude of the irrotational frontogenesis increasing as the surface cyclone amplified.

For the case considered, partitioned geostrophic \mathbf{Q} vector “forcing” for vertical motion revealed approximately equal contributions from the upper-tropospheric PV anomalies and the near-surface thermal perturbations.

Characteristic patterns of \mathbf{Q} vectors and \mathbf{Q} -vector divergence are identified and presented for cases including an upper trough interacting with a surface baroclinic zone and a propagating surface edge wave.

1. Introduction

While the principle kinematic mechanisms for atmospheric frontogenesis are well understood (deformation, divergence, and vorticity acting on a preexisting thermal gradient lead to changes in the magnitude and orientation of that gradient), and while it is generally understood that the effects of the large-scale flow on frontal structure and evolution are important [Schultz et al. (1998) and references therein], a fundamental question remains unaddressed: How might those kinematic properties of the wind field be attributed to specific disturbances [e.g.,

upper troughs, interior potential vorticity (PV) anomalies, surface thermal perturbations] of the observed flow?

Piecewise PV inversion allows for the attribution of particular features of the wind and mass fields to specific portions of the three-dimensional PV field. To date, most applications of the inversion of PV have focused on diagnosing the development of extratropical cyclones. These studies include Davis and Emanuel (1991), Davis (1992a,b), Davis et al. (1993), Black and Dole (1993), Hakim et al. (1996), Nielsen-Gammon and Lefevre (1996), Davis et al. (1996), and Bresky and Colucci (1996).

Nielsen et al. (1991) first suggested that piecewise PV inversion might be used in the diagnosis of frontogenesis. In that study, Nielsen et al. qualitatively demonstrated that the wind field attributed to lower-tropospheric PV anomalies had kinematic properties that supported upper-tropospheric frontogenesis along the dynamic tropopause. Davies et al. (1991) considered frontal evolution

Corresponding author address: Prof. Michael C. Morgan, University of Wisconsin—Madison, 1225 West Dayton St., Madison, WI 53706.
E-mail: morgan@meteor.wisc.edu

in a uniform PV atmosphere and qualitatively described the evolution of frontal structures at the boundaries in terms of the boundary thermal perturbations. Ramos (1997) and Korner (1998) have demonstrated the efficacy of quantitatively applying the technique of piecewise PV inversion to the development of an upper-tropospheric and a surface front, respectively. To date, no extant published studies have attempted to quantitatively apply the techniques of piecewise PV inversion to the diagnosing of surface frontogenesis.

In this paper a new approach to understanding atmospheric frontogenesis is presented: the technique of piecewise PV inversion is employed to attribute particular kinematic and frontogenetic properties of the wind field to synoptically significant PV structures. The diagnosis of surface frontogenesis is accomplished using \mathbf{Q} vectors partitioned into parts associated with upper-, middle-, and lower-tropospheric PV. A review of tools used in diagnosing surface frontogenesis and performing piecewise PV inversions is provided in section 2. The technique of piecewise PV partitioning of the \mathbf{Q} vector is presented in section 3. Diagnostic applications of the technique are demonstrated in a case study of observed cyclogenesis and attendant frontogenesis in section 4. An additional application of the piecewise PV partitioning of the \mathbf{Q} vector to vertical motion diagnosis is presented in section 5. A summary and discussion of results are contained in section 6.

2. Basic diagnostic tools

a. The scalar and vector frontogenesis functions and \mathbf{Q} vectors

Frontogenesis associated with the two-dimensional wind field on a quasi-horizontal surface may be diagnosed using the two-dimensional scalar frontogenesis function F_n (Petterssen 1936),

$$\begin{aligned} F_n &\equiv \frac{d}{dt} |\nabla\theta| \\ &= \frac{1}{|\nabla\theta|} \left[- \left(\frac{\partial\theta}{\partial x} \right)^2 \frac{\partial u}{\partial x} - \frac{\partial\theta}{\partial y} \frac{\partial\theta}{\partial x} \frac{\partial v}{\partial x} - \frac{\partial\theta}{\partial x} \frac{\partial\theta}{\partial y} \frac{\partial u}{\partial y} - \left(\frac{\partial\theta}{\partial y} \right)^2 \frac{\partial v}{\partial y} \right] \\ &= \frac{|\nabla\theta|}{2} (D \cos 2\beta - \delta), \end{aligned} \quad (2.1)$$

where D is the resultant deformation, β the angle between the isentropes and the axis of dilatation, and δ the horizontal divergence. From (2.1) it can be seen that horizontal deformation contributes to frontogenesis in situations for which the axis of dilatation is within 45° of isentropes and that *convergence* acts frontogenetically independent of the orientation of $\nabla\theta$.

If the concept of frontogenesis is generalized to include the time rate of change of the orientation of the horizontal temperature gradient, a two-dimensional vector frontogenesis function \mathbf{F} , may be defined (Keyser et al. 1988):

$$\mathbf{F} = \frac{d}{dt} \nabla\theta = -F_n \hat{\mathbf{n}} + F_s \hat{\mathbf{s}}, \quad (2.2)$$

where F_s is defined by

$$F_s = \hat{\mathbf{n}} \cdot \left(\hat{\mathbf{k}} \times \frac{d}{dt} \nabla\theta \right) = \frac{|\nabla\theta|}{2} (D \sin 2\beta + \zeta), \quad (2.3)$$

ζ is the relative vorticity, and (s, n) represents a right-handed Cartesian coordinate system defined locally such that the n axis points toward cold air. The effect of horizontal deformation is to rotate the potential temperature gradient toward the axis of dilatation: (counter-) clockwise rotation when the isentropes lie within 90° (between 90° and 180°) of the axis of dilatation. (Anti-)Cyclonic relative vorticity acts to rotate the isentropes (anti-)cyclonically.

The vector frontogenesis function is closely related to the \mathbf{Q} vector, defined as the Lagrangian time rate of change of the horizontal potential temperature gradient following the horizontal fluid motion:

$$\mathbf{Q} \equiv \frac{d}{dt} \Big|_h \nabla\theta = - \left[\left(\frac{\partial \mathbf{v}}{\partial x} \cdot \nabla\theta \right) \hat{\mathbf{i}} + \left(\frac{\partial \mathbf{v}}{\partial y} \cdot \nabla\theta \right) \hat{\mathbf{j}} \right], \quad (2.4)$$

where the notation $(d/dt)_h$ denotes the time rate of change of a variable following the horizontal motion, \mathbf{v} .¹

Hoskins et al. (1978) and Hoskins and Pedder (1980) introduced and demonstrated the utility of the geostrophic \mathbf{Q} vector, \mathbf{Q}_g :

$$\mathbf{Q}_g \equiv \frac{d}{dt} \Big|_g \nabla\theta = - \left[\left(\frac{\partial \mathbf{v}_g}{\partial x} \cdot \nabla\theta \right) \hat{\mathbf{i}} + \left(\frac{\partial \mathbf{v}_g}{\partial y} \cdot \nabla\theta \right) \hat{\mathbf{j}} \right],$$

where the notation $(d/dt)_g$ denotes a time rate of change of a variable following the geostrophic motion, \mathbf{v}_g . It is easily shown that the \mathbf{Q} vector, proportional to the vector frontogenesis function, is also useful in the diagnosis of frontogenesis. We define \mathcal{F} , the \mathbf{Q} -vector frontogenesis:

$$\mathcal{F} \equiv \frac{\nabla\theta}{|\nabla\theta|} \cdot \frac{d}{dt} \nabla\theta = \frac{1}{2|\nabla\theta|} \frac{d}{dt} |\nabla\theta|^2 = \frac{\mathbf{Q} \cdot \nabla\theta}{|\nabla\theta|} = F_n. \quad (2.5)$$

Relation (2.5) states that if \mathbf{Q} points in the same direction as $\nabla\theta$, then the magnitude of the horizontal potential temperature gradient will increase. If the \mathbf{Q} vector is expressed in the local (n, s) coordinate system,

$$\mathbf{Q} = -Q_n \hat{\mathbf{n}} + Q_s \hat{\mathbf{s}} = \mathbf{Q}_n + \mathbf{Q}_s,$$

where $\mathbf{Q}_n = \mathbf{Q} \cdot \nabla\theta / |\nabla\theta|$, $\mathbf{Q}_s = \mathbf{Q} \cdot (\hat{\mathbf{k}} \times \nabla\theta) / |\nabla\theta|$, $\mathbf{Q}_n = -Q_n \hat{\mathbf{n}}$, and $\mathbf{Q}_s = Q_s \hat{\mathbf{s}}$, then it is seen that the component of \mathbf{Q} perpendicular to the isentropes, \mathbf{Q}_n , is as-

¹ Because $(d/dt)\nabla\theta$ has a contribution from the differential vertical advection of potential temperature, (2.4) is strictly valid for adiabatic, inviscid, horizontal ($\omega = 0$) flow. We choose to define \mathbf{Q} in this manner as we will be considering the effects of horizontal motions on the surface frontogenesis.

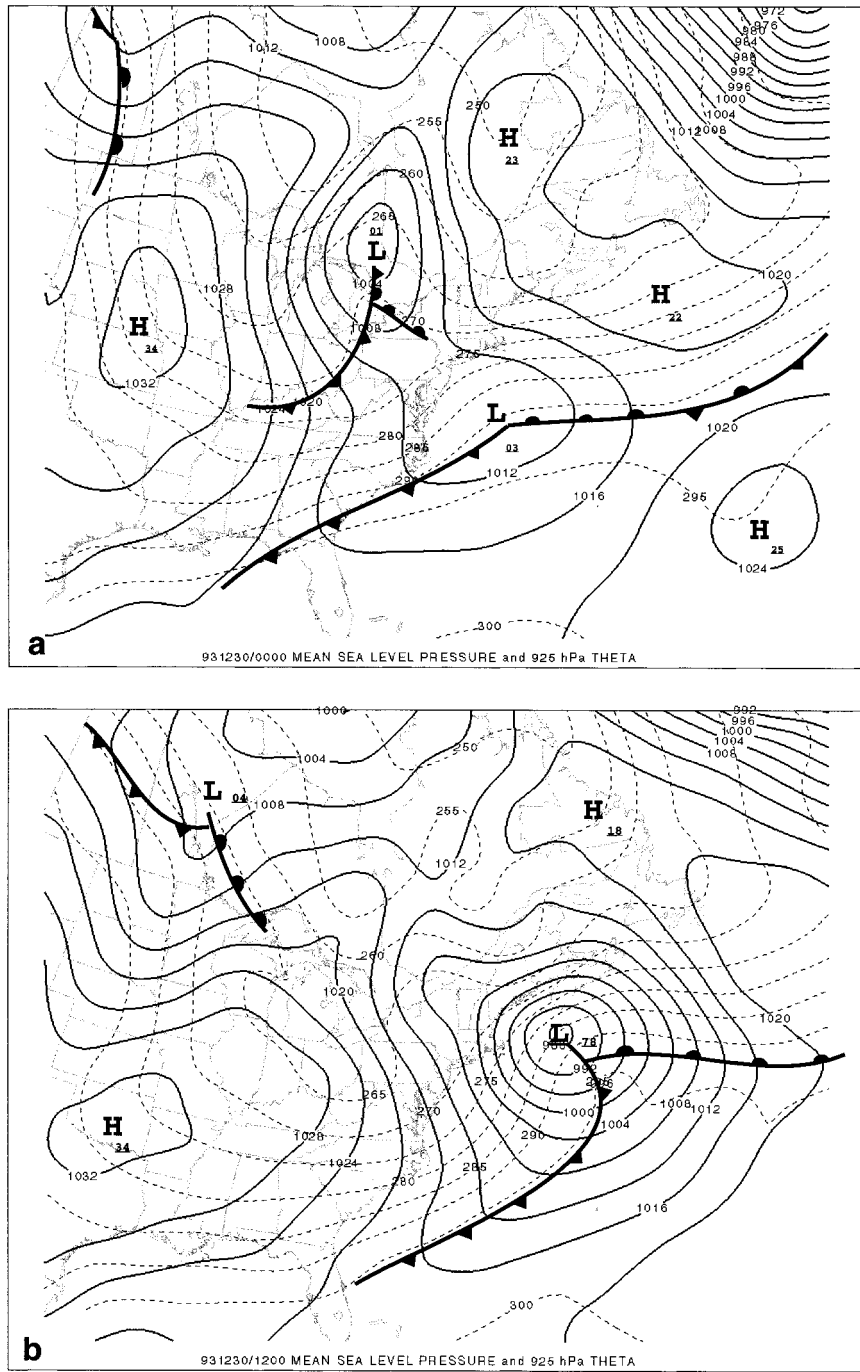


FIG. 1. Mean sea level pressure (solid contours, contour interval 4 hPa) and 925-hPa potential temperature (dashed contours, contour interval 5 K) at (a) 0000 UTC 30 Dec 1993, (b) 1200 UTC 30 Dec, and (c) 0000 UTC 31 Dec.

sociated with frontogenesis, while the component of \mathbf{Q} parallel to isentropes, Q_s , governs the rotation of the potential temperature gradient. For $\nabla\theta$ not parallel to \mathbf{Q}_s , $\nabla\theta$ will rotate toward the direction of the vector \mathbf{Q}_s .

Here \mathbf{Q}_g may also be used as a diagnostic of vertical

motion. Hoskins et al. (1978) show that mathematically, $\nabla \cdot \mathbf{Q}_g$ acts as a “forcing term” in the adiabatic, inviscid quasigeostrophic (QG) ω equation on an f plane:

$$\left(S\nabla^2 + \frac{f_0}{\gamma} \frac{\partial^2}{\partial p^2} \right) \omega = L(\omega) = -2\nabla \cdot \mathbf{Q}_g, \quad (2.6)$$

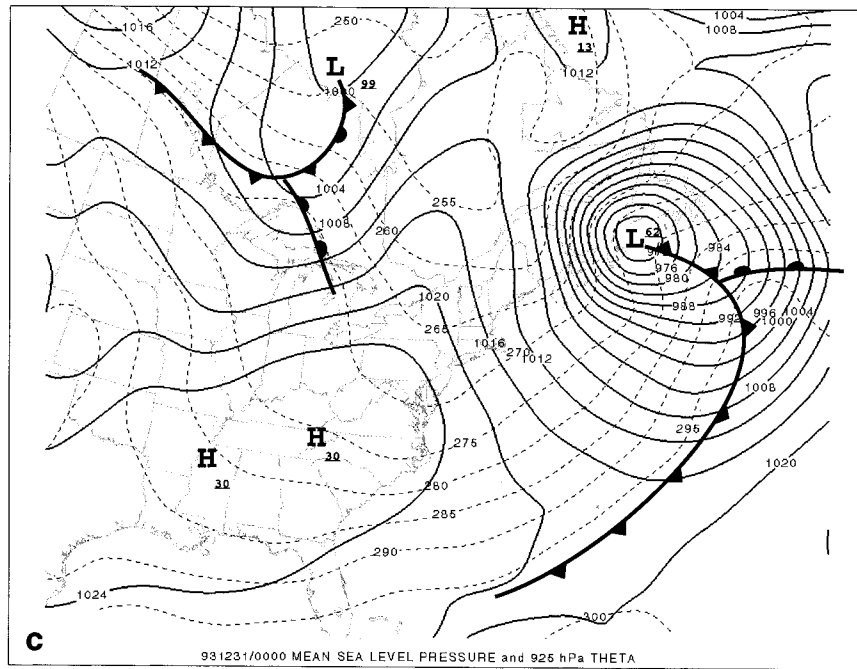


FIG. 1. (Continued)

where the operator L is given by $L = S\nabla^2 + (f_0/\gamma)(\partial^2/\partial p^2)$, ω is the vertical velocity in pressure coordinates, $S = -(T/\theta)(d/dp)\bar{\theta}$ is a static stability parameter, $(d/dp)\bar{\theta}$ is a reference state stratification, $\gamma = (R_d/p)(p/p_0)^\kappa$, and all other symbols have their standard meteorological meanings. Provided that L is elliptic, regions of \mathbf{Q}_g convergence (divergence) are associated with regions of ascent (descent).

b. PV inversion

Potential vorticity is a useful diagnostic quantity for the study of nearly balanced atmospheric flows. Its usefulness is linked to two fundamental concepts: the invertibility principle and PV conservation. The invertibility principle first considered by Kleinschmidt (1957) and described in detail in Hoskins et al. (1985) states that given a distribution of PV, a balance condition (a diagnostic relationship between the streamfunction, ψ , and geopotential, φ), and boundary conditions, the balanced wind and temperature fields associated with a particular PV distribution can be recovered.² In this paper, the balanced condition used is the nonlinear balance equation [also referred to as the Charney balance equation, Charney (1955)]:

² A more complete summary of details of the inversion process for observed PV distributions may be found in Davis and Emanuel (1991) and Bresky and Colucci (1996) for Ertel PV and Holopainen and Kaurola (1991) and Nielsen-Gammon and Lefevre (1996) for quasigeostrophic PV.

$$\nabla^2\varphi = \nabla \cdot (f\nabla\psi) + 2m^2\left(\frac{\partial^2\psi}{\partial x^2}\frac{\partial^2\psi}{\partial y^2} - \frac{\partial^2\psi}{\partial x\partial y}\frac{\partial^2\psi}{\partial x\partial y}\right), \quad (2.7)$$

where m is a map factor, and f , the Coriolis parameter. Davis et al. (1996) demonstrate that in areas where ageostrophic motions are comparable in magnitude to the observed winds (near jet streaks, frontal zones, and areas of significant curvature), the balanced flow described by the nonlinear balance equation captures more of the observed flow than geostrophic balance.

The PV used in the inversion is Ertel PV, q :

$$q \equiv \frac{1}{\rho}\boldsymbol{\omega}_a \cdot \nabla\theta,$$

where ρ is the density and $\boldsymbol{\omega}_a$ the absolute vorticity vector. Ertel PV is conserved for adiabatic, inviscid flow and this conservation is a property of the full primitive equations. We scale the definition of PV by assuming the nondivergent wind, $\mathbf{v}_\psi = \mathbf{k} \times \nabla\psi$, is much greater in magnitude than the irrotational wind and by neglecting the vertical velocity contribution to PV. The resulting expression for PV, assuming hydrostatic balance ($\partial\varphi/\partial\pi = -\theta$), is

$$q = \frac{g\kappa\pi m^2}{p} \left[\left(\frac{f}{m^2} + \nabla^2\psi \right) \frac{\partial^2\varphi}{\partial\pi^2} + \frac{\partial^2\varphi}{\partial\pi^2} \nabla^2\psi - \frac{\partial^2\psi}{\partial x\partial\pi} \frac{\partial^2\varphi}{\partial x\partial\pi} - \frac{\partial^2\psi}{\partial y\partial\pi} \frac{\partial^2\varphi}{\partial y\partial\pi} \right], \quad (2.8)$$

where $\pi = (p/p_0)^\kappa$ is the Exner function.

Given a distribution of PV, q , the equation set (2.7)

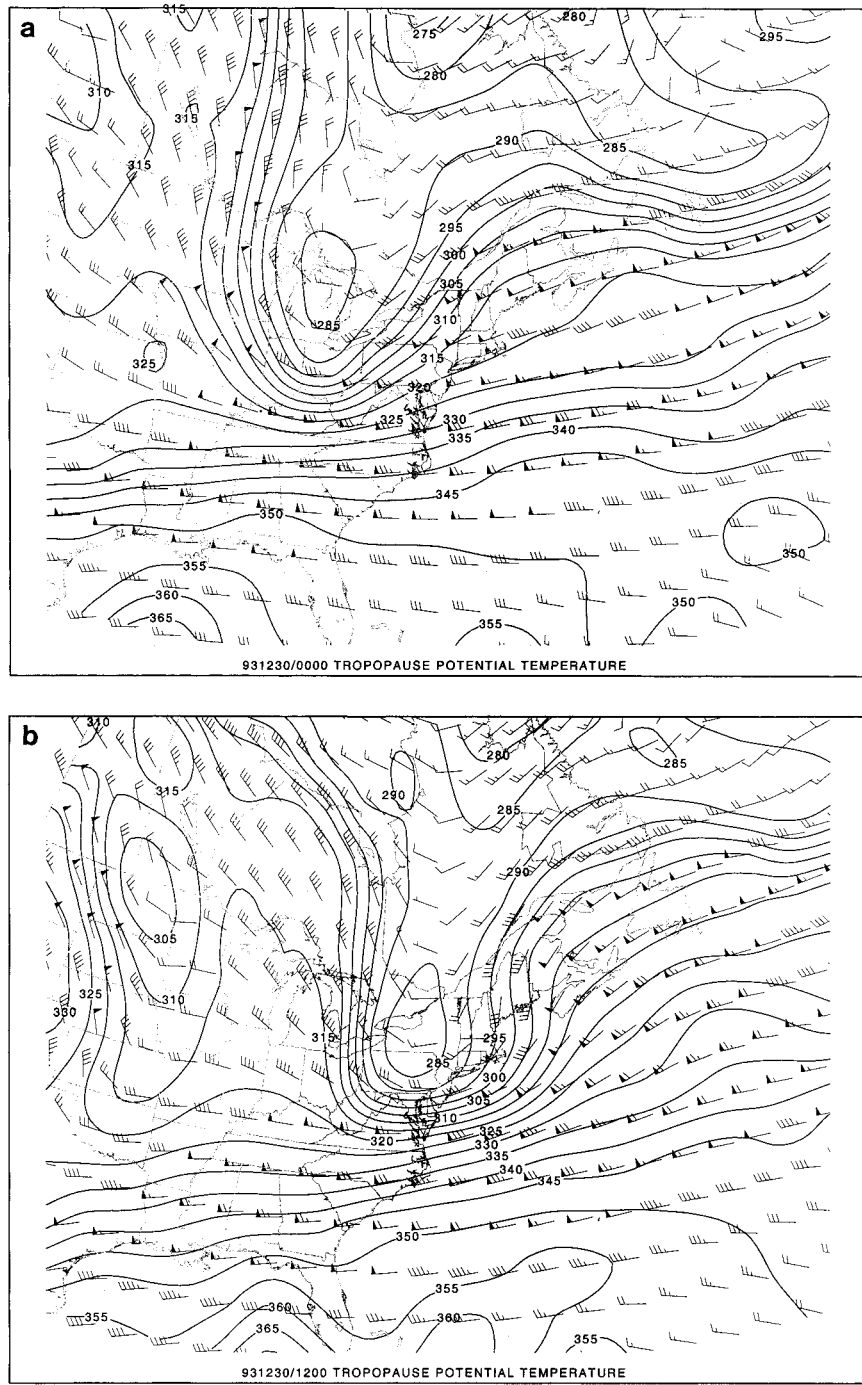


FIG. 2. Tropopause potential temperature (solid contours, contour interval 5 K) and wind (short barb = 5 m s⁻¹; long barb = 10 m s⁻¹; pennant = 50 m s⁻¹) at (a) 0000 UTC 30 Dec 1993, (b) 1200 UTC 30 Dec, and (c) 0000 UTC 31 Dec.

and (2.8), along with boundary conditions constitutes a statement of invertibility: the full (unpartitioned) balanced flow associated with an observed distribution of PV can be recovered through solution of this system. Neumann boundary conditions ($\partial\phi/\partial\pi = f_0\partial\psi/\partial\pi = -\theta$) are applied at $\pi = \pi_0$ (lower boundary) and $\pi =$

π_T (upper boundary) while Dirichlet boundary conditions are specified on the lateral boundaries.

c. Piecewise PV inversion

Davis and Emanuel describe a technique known as *piecewise PV inversion*, wherein the three-dimensional

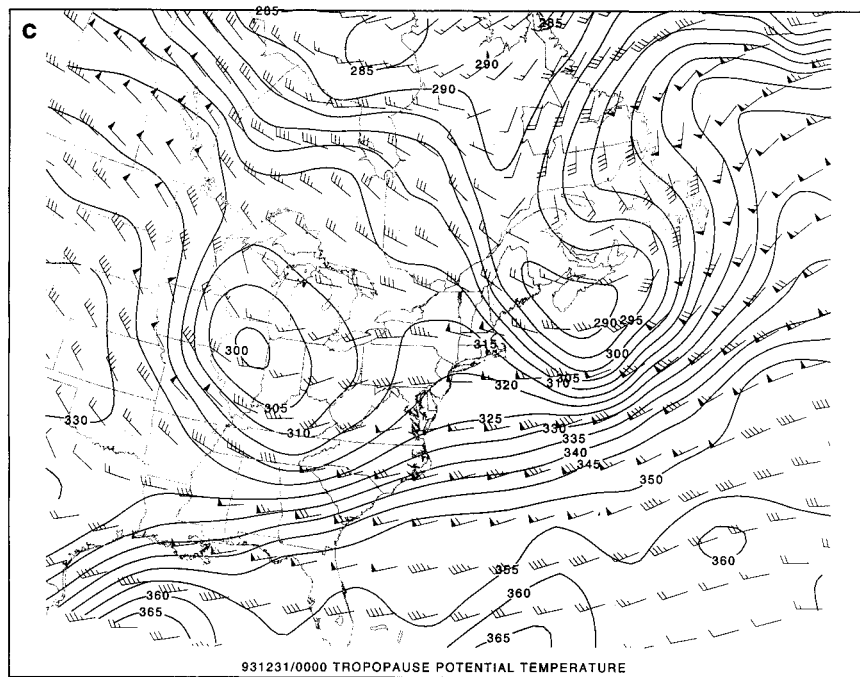


FIG. 2. (Continued)

PV field is divided into mean and perturbation fields, and separate portions of the perturbation PV field (q'_k) are inverted individually to determine both the balanced perturbation geopotential height (φ'_k) and streamfunction (ψ'_k) attributed to q'_k . The nonlinearity of the nonlinear balance equation results in a nonuniqueness in the attributions of φ'_k and ψ'_k to q'_k . Davis (1992a) provides a detailed discussion of this issue. We adopt the method proposed and implemented by Davis and Emanuel, Davis (1992b), and Davis et al. (1996): linearize (2.7) and (2.8) about a basic state that is the average of the mean and total balanced flow. The resulting equations are

$$\nabla^2 \varphi'_k = \nabla \cdot (f \nabla \psi'_k) + 2m^2 \left(\frac{\partial^2 \tilde{\psi}}{\partial x^2} \frac{\partial^2 \psi'_k}{\partial y^2} + \frac{\partial^2 \tilde{\psi}}{\partial y^2} \frac{\partial^2 \psi'_k}{\partial x^2} - 2 \frac{\partial^2 \tilde{\psi}}{\partial x \partial y} \frac{\partial^2 \psi'_k}{\partial x \partial y} \right), \quad (2.9)$$

and

$$q'_k = \frac{g \kappa \pi m^2}{p} \left[\left(\frac{f}{m^2} + \nabla^2 \tilde{\psi} \right) \frac{\partial^2 \varphi'_k}{\partial \pi^2} + \frac{\partial^2 \tilde{\varphi}}{\partial \pi^2} \nabla^2 \psi'_k - \frac{\partial^2 \tilde{\psi}}{\partial x \partial \pi} \frac{\partial^2 \varphi'_k}{\partial x \partial \pi} - \frac{\partial^2 \tilde{\varphi}}{\partial x \partial \pi} \frac{\partial^2 \psi'_k}{\partial x \partial \pi} - \frac{\partial^2 \tilde{\psi}}{\partial y \partial \pi} \frac{\partial^2 \varphi'_k}{\partial y \partial \pi} - \frac{\partial^2 \tilde{\varphi}}{\partial y \partial \pi} \frac{\partial^2 \psi'_k}{\partial y \partial \pi} \right], \quad (2.10)$$

where $(\tilde{\cdot}) = (\overline{\cdot}) + (\cdot)'/2$. An advantage of this ap-

proach is that the resulting flow fields associated with φ'_k and ψ'_k are linearly superposable such that the sum of the individual perturbation fields is equal to the total perturbation field.

The upper and lower boundary conditions are $(\partial/\partial \pi) \tilde{\varphi}_k = f(\partial/\partial \pi) \tilde{\psi}_k = -\theta_k$ at $\pi = \pi_0$ and $\pi = \pi_T$. Because perturbation wind along the lateral boundaries of the inversion domain may be attributed to PV anomalies within and without the domain, lateral boundary conditions are difficult to determine. We apply homogeneous boundary conditions for φ'_k and ψ'_k along the lateral boundaries and choose the domain size larger than the region of interest. Inversions were performed on domains of varying sizes and the solutions did not appreciably change.

Having solved for ψ'_k , the nondivergent velocity field associated with q'_k may be computed: $\mathbf{v}'_k = \mathbf{k} \times \nabla \psi'_k$. The perturbation geostrophic velocity \mathbf{v}'_{gk} may also be obtained: $\mathbf{v}'_{gk} = \hat{\mathbf{k}}/f \times \nabla \varphi'_k$. The attributed wind fields can then be added to recover the total balanced, horizontal flow. By calculating the balanced flow associated with individual PV perturbations, one can identify how each PV anomaly contributes to the flow at any level within the atmosphere.

While the partitioning of the PV distribution is arbitrary, for the interpretation of partitioning to be effective, one must identify a minimum number of pieces of PV that are subjectively associated with the most important PV variations. Morgan and Nielsen-Gammon (1998) and references therein demonstrate that the PV distribution in the troposphere and lower stratosphere is simple: most of the significant variations in PV are found near the tropopause associated with tropopause undulations and near the earth's

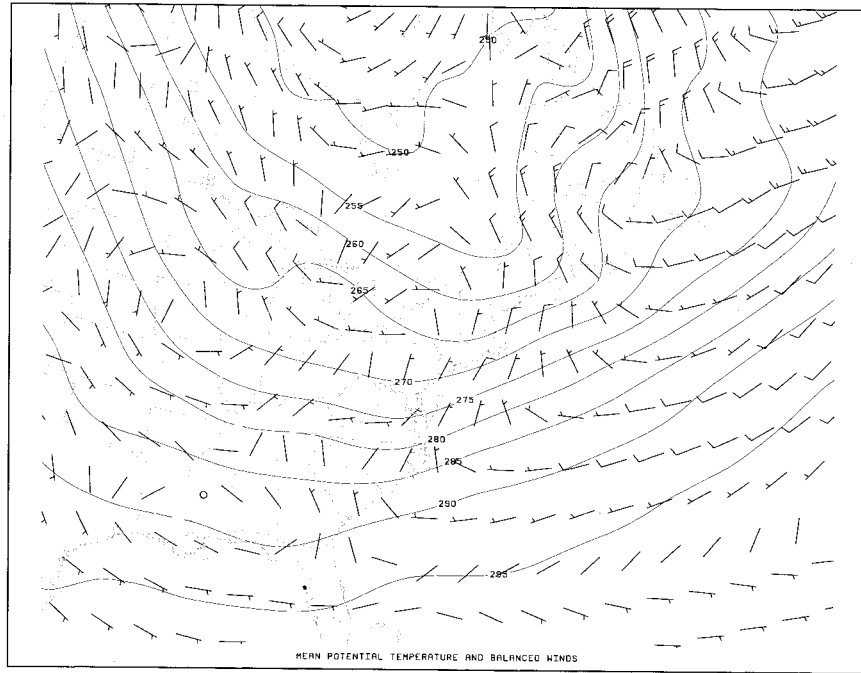


FIG. 3. The 925-hPa time-mean balanced winds (short barb = 5 m s⁻¹ and long barb = 10 m s⁻¹) and time-mean potential temperature (contour interval 5 K).

surface in the form of boundary temperature variations. Within the middle and lower troposphere and the lower stratosphere, PV anomalies are generally small and non-systematic with the exception of those anomalies locally generated from nonconservative effects.

We choose to divide the nondivergent flow into parts attributed to a time-mean PV distribution (\mathbf{v}_{mean}) and to deviations from that time mean associated with upper-tropospheric, middle- and lower-tropospheric, and boundary (near-surface potential temperature) PV. These parts are denoted \mathbf{v}'_u , \mathbf{v}'_m , and \mathbf{v}'_l , respectively. The irrotational part of the flow, $\mathbf{v}_\chi = \nabla\chi$, where χ is the velocity potential, which does not satisfy the nonlinear balance equation, as well as the vertical velocity, ω , may be determined by solving the prognostic balance system. The prognostic balance system comprises four equations and four unknowns: the time tendencies of the streamfunction and velocity potential, an ω equation, and the mass continuity equation (Davis and Emanuel 1991).

3. Piecewise diagnosis of frontogenesis

Having performed a piecewise PV inversion to determine the wind field attributed to specific pieces of the observed PV distribution, we may determine how each piece of that PV distribution contributes to the frontogenesis. While both the perturbation temperature and wind fields can be attributed to specific parts of the observed PV distribution, we choose to treat *the observed temperature distribution as given*, and use only the attributed perturbation wind field in our partitioned

frontogenesis diagnosis, because our concern in this study is identifying the *kinematic* and frontogenetic properties of the wind field at a given level due to PV anomalies local to and remote from that level. We propose two different techniques that allow for the quantitative diagnosis of the contributions of various parts of a PV distribution to the total horizontal frontogenesis.

a. Partitioning of the two-dimensional frontogenesis function, F_n

Based on the piecewise PV partitioning described in the previous section, the two-dimensional, balanced frontogenesis function, F , may be separated into five components:

$$F_n^k = \mathcal{F}^k = \frac{1}{|\nabla\theta|} \left[- \left(\frac{\partial\theta}{\partial x} \right)^2 \frac{\partial}{\partial x} u'_k - \frac{\partial\theta}{\partial y} \frac{\partial\theta}{\partial x} \frac{\partial}{\partial x} v'_k - \frac{\partial\theta}{\partial x} \frac{\partial\theta}{\partial y} \frac{\partial}{\partial y} u'_k - \left(\frac{\partial\theta}{\partial y} \right)^2 \frac{\partial}{\partial y} v'_k \right],$$

where ($k = 1, \dots, 5$). For ease in describing each of the components of this partitioning, we will henceforth identify each contribution with the superscript u , m , l , mean, or χ each representing the respective contributions attributable to the upper-, middle-, and lower-tropospheric, and mean PV and the irrotational part of the flow. Thus, \mathcal{F}^u represents the frontogenesis associated with perturbation winds attributed to upper-tropospheric PV. A partitioning of this form was first performed by

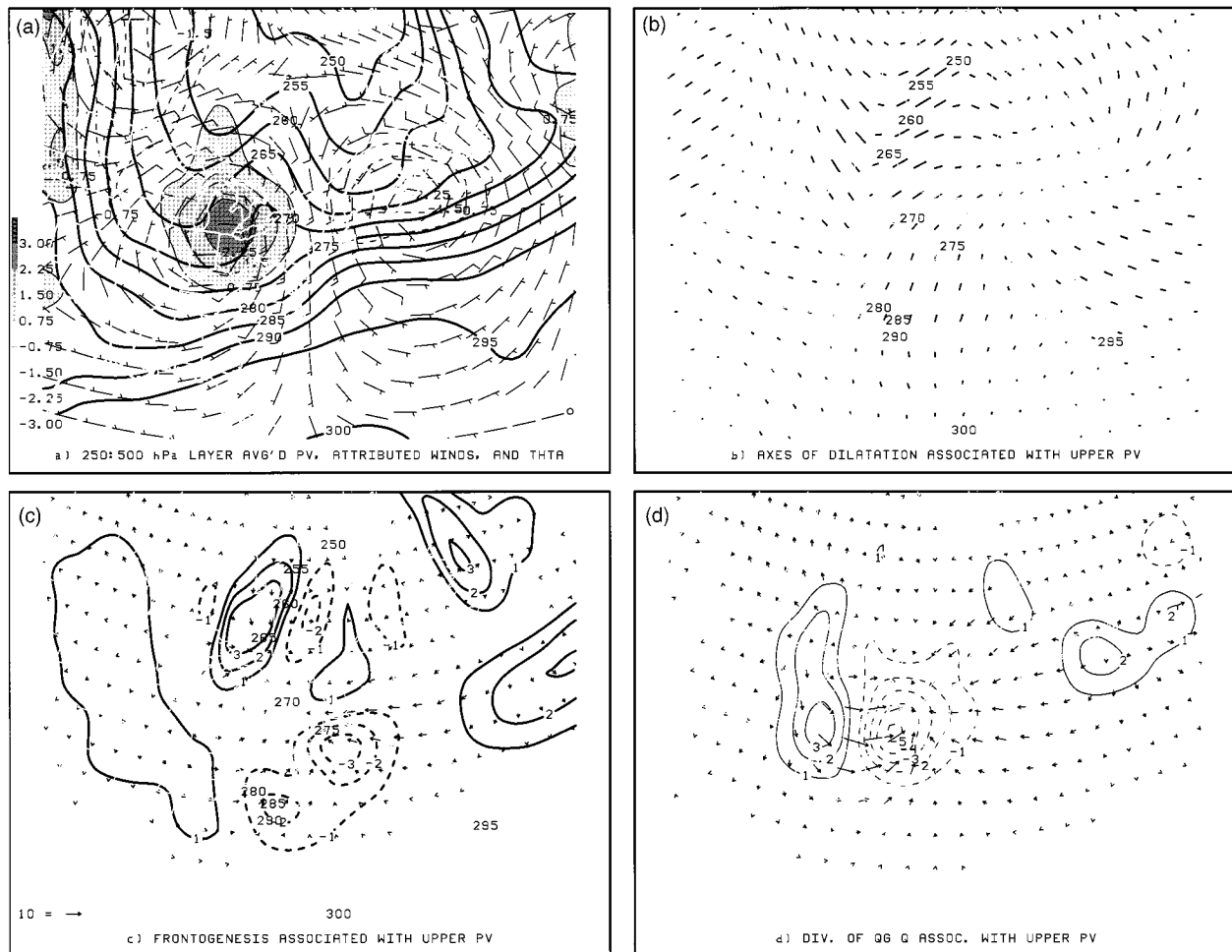


FIG. 4. The 925-hPa potential temperature (solid, heavy contour, interval 5 K) and (a) 925-hPa winds attributed to upper-tropospheric PV anomalies (short barb = 5 m s⁻¹ and long barb = 10 ms⁻¹) with 250–500-hPa-layer-averaged PV anomalies (contoured and shaded, contour interval 0.75 PVU, negative values dashed), (b) 925-hPa dilatation axes (lengths are proportional to the total deformation) for winds attributed to the upper-tropospheric PV anomalies (maximum deformation 7.1 × 10⁻⁵ s⁻¹), (c) 925-hPa balanced **Q** vectors and **Q**-vector frontogenesis [heavy contoured, negative values dashed, contour interval 1 K (1000 km)⁻¹ (3 h)⁻¹] attributed to the upper-tropospheric PV anomalies, and (d) 500–850-hPa-layer-averaged geostrophic **Q** vectors and geostrophic **Q**-vector convergence (contour, interval 1 × 10⁻¹⁵ K m⁻² s⁻¹) attributed to the upper-tropospheric PV anomalies for 0000 UTC 30 Dec 1993.

Ramos (1997) in a study of upper-tropospheric frontogenesis along the dynamic tropopause and more recently by Korner (1998) in a study of surface frontogenesis. We note that the components of frontogenesis are linear in the velocity fields, and as a consequence, one may linearly superpose the contributions, \mathcal{F}^u , \mathcal{F}^m , \mathcal{F}^l , $\mathcal{F}^{\text{mean}}$, and \mathcal{F}^x to perform a budget of the total frontogenesis: We note that because this partitioning is also linear in the velocity field: $\mathcal{F} = \mathcal{F}^u + \mathcal{F}^m + \mathcal{F}^l + \mathcal{F}^{\text{mean}} + \mathcal{F}^x$.

*b. A piecewise PV partitioning of the **Q** vector and **Q**-vector frontogenesis*

Because the **Q** vector is also linear in the horizontal velocity, **v**, we may separate the **Q** vector into parts as was done for the frontogenesis:

$$\mathbf{Q}^k = - \left[\left(\frac{\partial}{\partial x} \mathbf{v}'_k \cdot \nabla \theta \right) \hat{\mathbf{i}} + \left(\frac{\partial}{\partial y} \mathbf{v}'_k \cdot \nabla \theta \right) \hat{\mathbf{j}} \right].$$

The parts are denoted \mathbf{Q}^u , \mathbf{Q}^m , \mathbf{Q}^l , \mathbf{Q}^{mean} , and \mathbf{Q}^x . We also define the following components of frontogenesis:

$$\mathcal{F}^k = \frac{\mathbf{Q}^k \cdot \nabla \theta}{|\nabla \theta|}. \tag{3.1}$$

When the velocity field used in the diagnosing \mathcal{F} is \mathbf{v}_ψ , the frontogenesis diagnosed is due entirely to deformation since by definition $\nabla \cdot \mathbf{v}_\psi = 0$.

4. Case study

The case chosen to demonstrate the proposed technique is a rapidly developing extratropical marine cy-

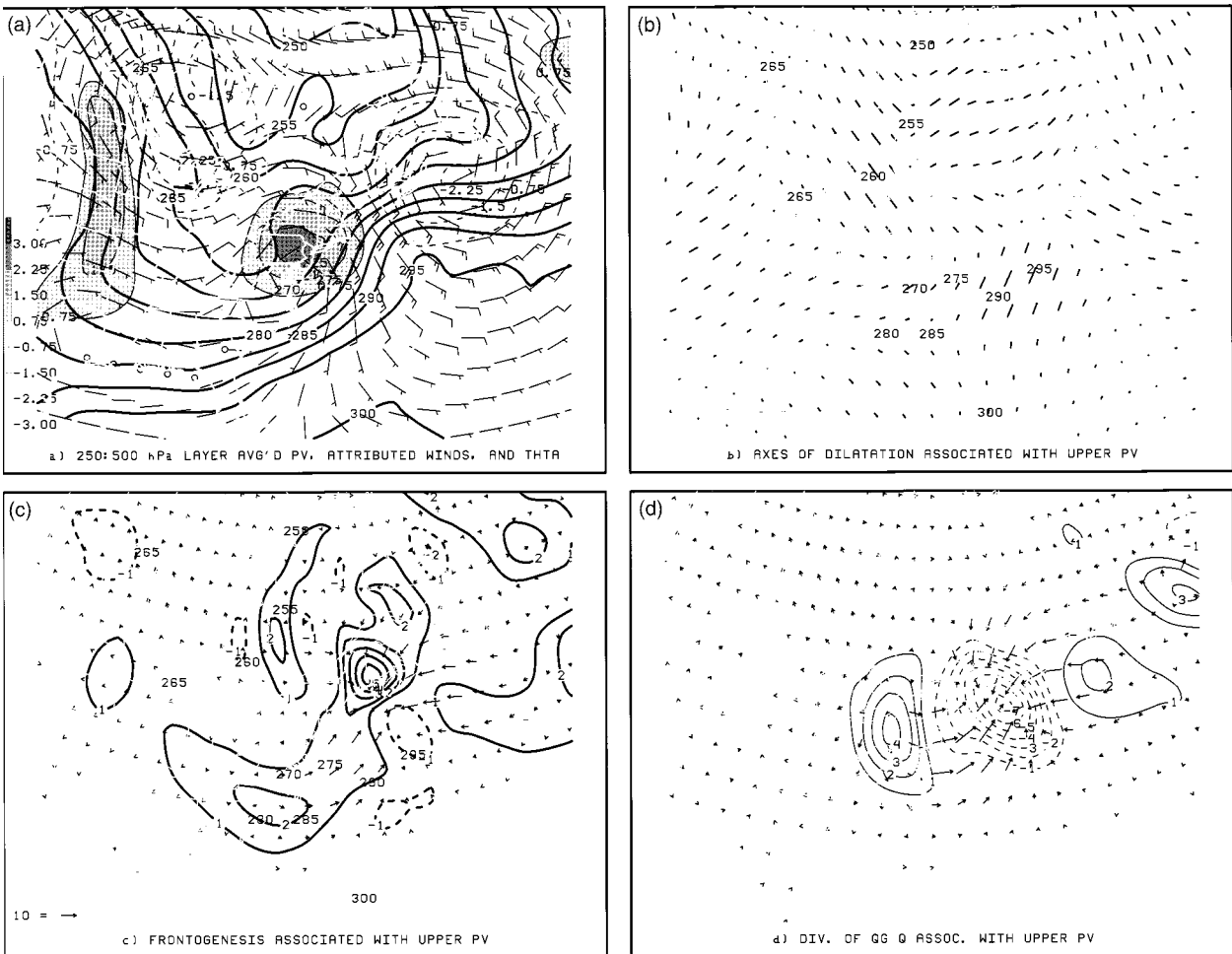


FIG. 5. As in Fig. 4 except for 1200 UTC 30 Dec 1993. Maximum deformation $6.9 \times 10^{-5} \text{ s}^{-1}$.

clone and attendant fronts resulting from the interaction of an upper-tropospheric mobile trough with a lower-tropospheric baroclinic zone. The case is also described in Morgan and Nielsen-Gammon (1998). Here only a cursory description of the event is provided. The data used in the analyses and diagnostic calculations are derived from the National Meteorological Center (NMC, now National Centers for Environmental Prediction) global analyses.³ While this dataset is insufficient to resolve detailed frontal structure, it will adequately resolve the properties of the larger-scale flow responsible for initiating frontogenesis. Surface and ship observations were subjectively analyzed to determine the in-

tensity of the offshore cyclone as well as the location of the attendant surface fronts.

a. Case description

The evolution of the 925-hPa potential temperature, mean sea level pressure, and surface frontal positions is shown in Fig. 1. At 0000 UTC 30 December 1993 the developing cyclone is manifest as a surface frontal wave located offshore of the Maryland coast with a minimum mean sea level pressure of 1003 hPa along a frontal zone extending from the Gulf of Mexico to offshore of the mid-Atlantic coast (Fig. 1a). During the 36-h preceding this time, a series of weak frontal cyclones had developed and propagated along the front. The lower-tropospheric thermal field was characterized by a small amplitude thermal ridge collocated with the minimum central pressure. At the same time, the analyses of potential temperature along the dynamic tropopause revealed an east-southeastward propagating short-wave trough located over northwestern Ohio and southeastern Michigan (Fig. 2a).

³ The NMC global analyses used in this section are prepared and maintained as DS082.0 by the Data Support Section, Scientific Computing Division, National Center for Atmospheric Research (NCAR). NCAR is operated by the University Corporation for Atmospheric Research and is sponsored by the National Science Foundation. The analyses are at $2.5^\circ \times 2.5^\circ$ resolution on the 1000-, 850-, 700-, 500-, 400-, 300-, 250-, 200-, 150-, 100-hPa surfaces.

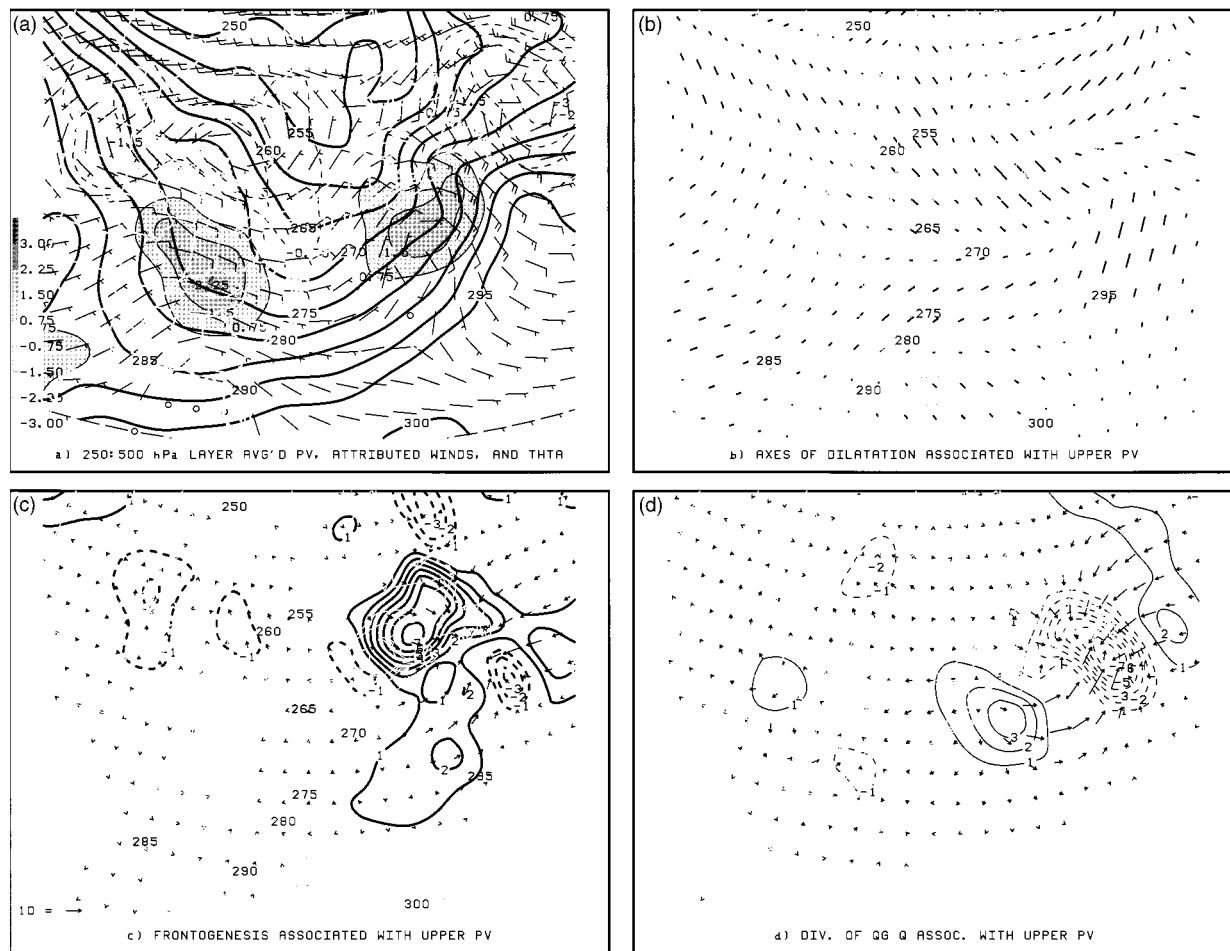


FIG. 6. As in Fig. 4 except for 0000 UTC 31 Dec 1993. Maximum deformation $8.0 \times 10^{-5} \text{ S}^{-1}$.

By 1200 UTC 30 December (Fig. 1b) the cyclone had deepened to 977 mb and was located to the south of Cape Sable, Nova Scotia. The surface thermal ridge had amplified considerably during this time interval—with the surface cyclone located at the crest of the thermal ridge. Moderate to heavy snowfall rates had been reported by many observing stations northwest of the cyclone track in the 12 h ending at this time. The surface cold front was, at this time, better defined, and the surface cyclone had begun to occlude. The upper trough was located in eastern Pennsylvania (Fig. 2b) and had not undergone any significant amplification. The ridge downstream of this trough had not amplified either.

The occluded cyclone continued its rapid deepening in the succeeding 12 h—reaching a minimum pressure of 962 hPa by 0000 UTC 31 December (Fig. 1c). At the tropopause (Fig. 2c), the upper trough had begun to wrap up cyclonically and the downstream ridge had undergone considerable amplification. Based upon the analyses of lower-tropospheric PV and tropopause potential temperature, Morgan and Nielsen-Gammon (1998) suggest that the ridge building is enhanced by

diabatic processes occurring in the precipitation shield northwest of the cyclone.

b. Piecewise PV inversion diagnosis of the partitioned wind field, Q vector, and Q-vector frontogenesis

We define the perturbation PV to be the departure of the observed PV from a 5-day mean centered on 29 December 1993. The 925-hPa time-mean potential temperature and balanced winds are shown in Fig. 3. The largest winds in the time mean are found in the northeast quadrant of the map where there had previously been a large-scale cyclonic circulation at the beginning of the 5-day period from which the mean had been computed. Over the region in which the cyclone described in this paper developed, the 925-hPa wind field is characterized by cyclonic curvature and winds of no more than 5 m s^{-1} in magnitude. In the time mean, a baroclinic zone extends from the southeast coast of the United States northeastward into the Atlantic.

We choose to partition the PV into four parts: a part

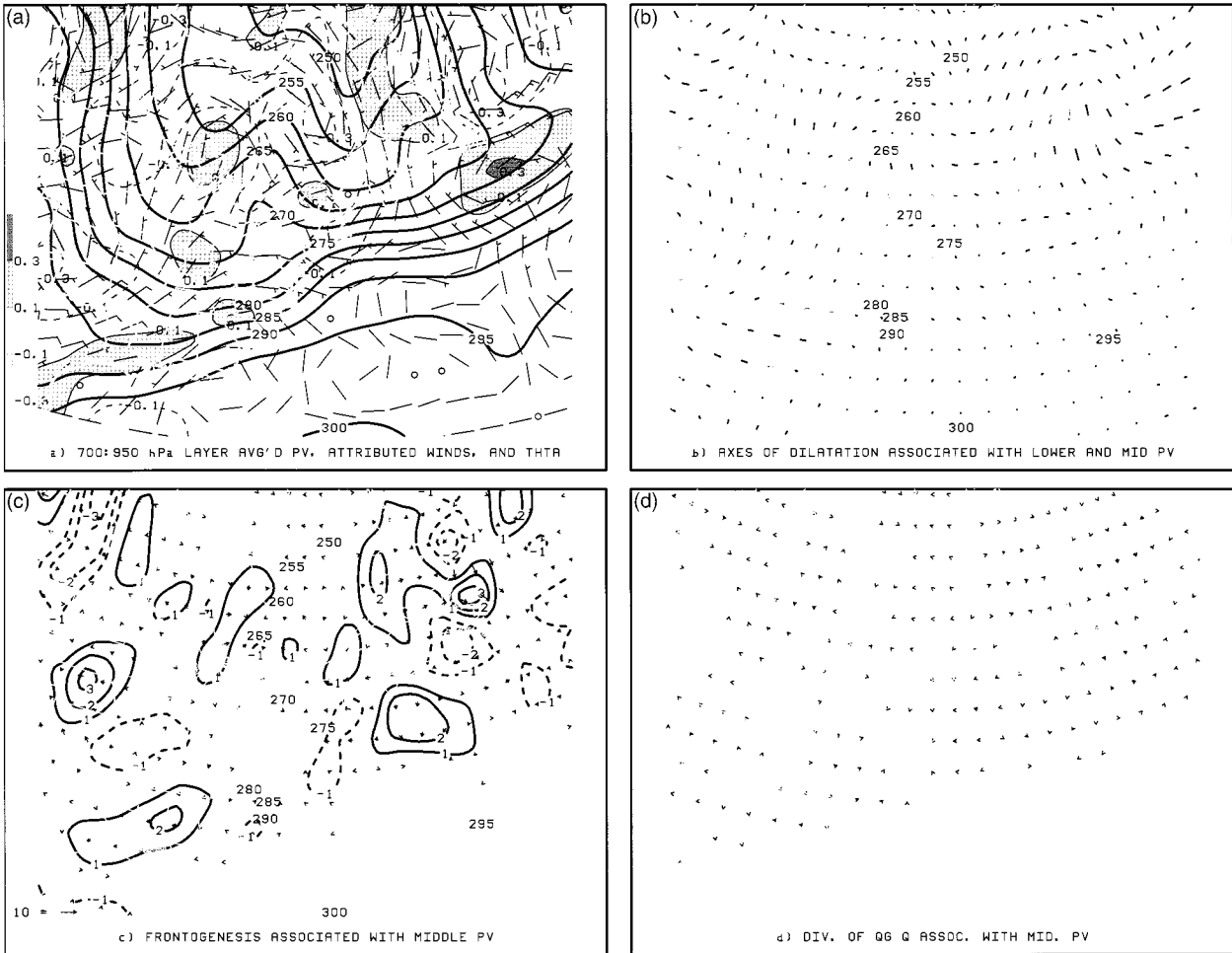


FIG. 7. The 925-hPa potential temperature (solid, heavy contour, interval 5 K) and (a) 925-hPa winds attributed to middle and lower-tropospheric PV anomalies (short barb = 5 m s⁻¹ and long barb = 10 m s⁻¹) with 700–850-hPa-layer-averaged PV anomalies (contoured and shaded, contour interval 0.3 PVU, negative values dashed), (b) 925-hPa dilatation axes for winds attributed to middle and lower-tropospheric PV anomalies (maximum deformation $4.7 \times 10^{-5} \text{ s}^{-1}$), (c) 925-hPa balanced \mathbf{Q} vectors and \mathbf{Q} -vector frontogenesis [heavy contoured, negative values dashed, contour interval 1 K (1000 km)⁻¹ (3 h)⁻¹] attributed to middle and lower-tropospheric PV anomalies, and (d) 500–850-hPa-layer-averaged geostrophic \mathbf{Q} vectors and geostrophic \mathbf{Q} -vector convergence (contour, interval $2 \times 10^{-15} \text{ K m}^{-2} \text{ s}^{-1}$) attributed to middle- and lower-tropospheric PV anomalies for 0000 UTC 30 Dec 1993.

associated with the upper boundary (125 hPa) potential temperature and upper-tropospheric PV (PV between and including 150 hPa and 500 hPa), q'_u ; a part associated with the small, interior PV variations (PV between 500 and 925 hPa), q'_m ; a part associated with near-surface (925 hPa) potential temperature variations, q'_l ; and a part associated with the 5-day time-mean distribution, q_{mean} . The inversions are performed in a rectangular domain on a cylindrical equidistant grid whose areal extent is defined by a southwestern grid point located at 25°N, 120°W and a northeastern grid point located at 65°N, 30°W.

In this subsection, we verify that the recovered perturbation wind fields are consistent with the observed perturbation PV distribution, qualitatively describe the frontogenetic potentialities of the perturbation wind fields by examining the perturbation winds and asso-

ciated axes of dilatation along with the 925-hPa potential temperature distribution, and quantitatively diagnose the partitioned frontogenesis using expression (3.1). In Figs. 4–12 the upper-left panels show the perturbation PV (q'_u , q'_m , or, q'_l) and that perturbation PV's attributed wind field overlying the 925-hPa potential temperature. The upper-right panels feature the dilatation axes of the attributed flow. The lower left show the corresponding distributions of perturbation \mathbf{Q} and \mathcal{F} , while \mathbf{Q}_g and the divergence of \mathbf{Q}_g are displayed in the lower-right panels.

1) FRONTOGENETIC CHARACTERISTICS OF THE UPPER PV ANOMALY

At 0000 UTC 30 December the cyclonic circulation associated with the upper trough over Michigan is ev-

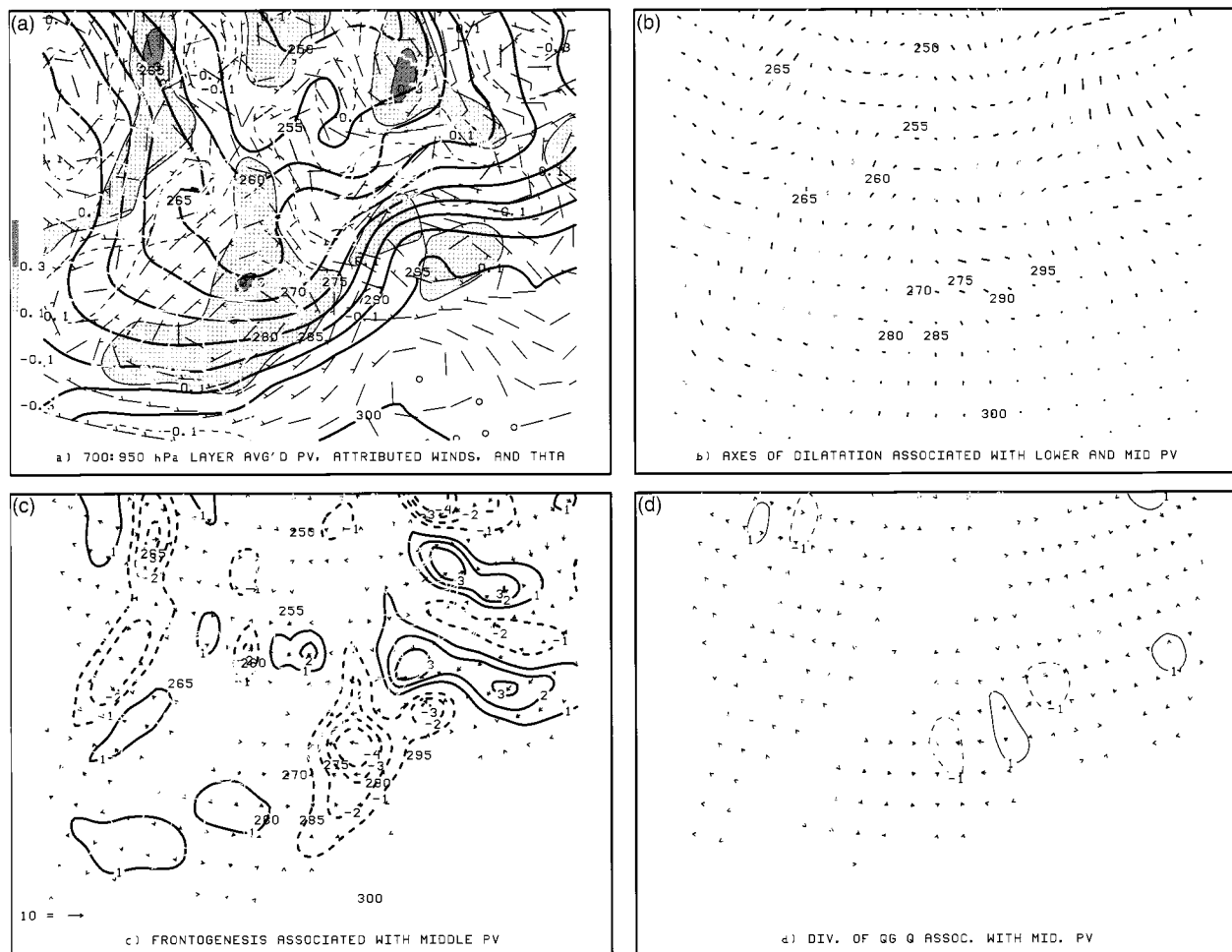


FIG. 8. As in Fig. 7 except for 1200 UTC 30 Dec 1993. Maximum deformation $4.4 \times 10^{-5} \text{ s}^{-1}$.

ident over the Great Lakes (Fig. 4a). A strong southerly flow at 925 hPa exists between the upper trough and the downstream ridge (manifest as the negative PV anomaly centered south of Nova Scotia). The wind attributed to the q'_u is tending to amplify the 925-hPa thermal ridge slightly west of the ridge axis. Because the dilatation axes of \mathbf{v}'_u are nearly perpendicular to the isentropes, frontolysis is expected along the mid-Atlantic and southeast coasts (Fig. 4b).

Here \mathbf{Q}'' is largest in the vicinity of the lower thermal wave where the thermal gradients are large and the perturbation balanced flow is maximized (Fig. 4c). Also, \mathbf{Q}'' is nearly parallel to the isentropes—oriented so as to point in the direction of the thermal ridge axis. Because of this orientation, one would diagnose an amplification of the thermal ridge, as the component of \mathbf{Q}'' along the isotherms indicates the change in the direction of the potential temperature gradient, $\nabla\theta$. Note that $\mathcal{F}'' < 0$ along the axis of the thermal ridge as there is a small component of \mathbf{Q}'' pointing opposite $\nabla\theta$. Referring back to Fig. 4b, we see that there is stretching deformation occurring in the ridge—asso-

ciated with $\mathcal{F}'' < 0$. Farther east, along the developing warm front, $\mathcal{F}'' > 0$ in the region south of the upper anticyclonic PV anomaly where the axis of dilatation of the flow is nearly parallel to the isentropes (Figs. 4b and 4c).

By 1200 UTC 30 December the positive q'_u characterizing the upper trough is located over Pennsylvania while the negative anomaly formerly located south of Nova Scotia is located farther east (Fig. 5a). A southeast flow, nearly in phase with the thermal ridge is observed between these two anomalies. The broad southeast flow weakens in eastern Maine where the 925-hPa \mathbf{v}'_u becomes diffluent and the axes of dilatation become nearly parallel to the isentropes (Fig. 5b).

At this time \mathbf{Q}'' has increased significantly in magnitude as a consequence of the magnitudes of both $\nabla\theta$ and \mathbf{v}'_u having increased (Fig. 5c). Also \mathbf{Q}'' remains largely oriented parallel to the isentropes—indicating a propensity of the 925-hPa flow associated with the upper trough to rotate isentropes so as to amplify the thermal ridge. Cold and warm frontogenesis is diagnosed as the component of \mathbf{Q}'' normal to the isentropes (Q''_n locally points

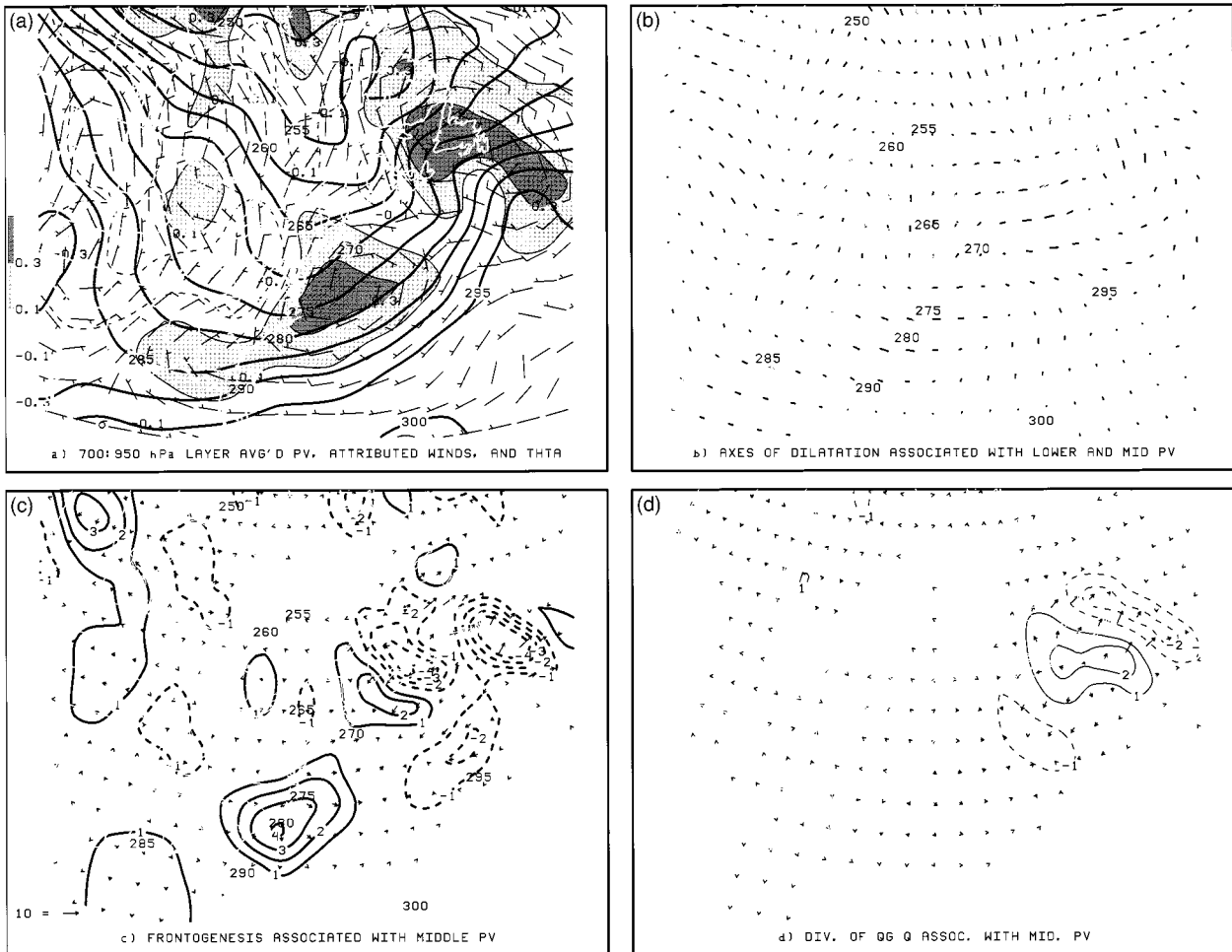


FIG. 9. As in Fig. 7 except for 0000 UTC 31 Dec 1993. Maximum deformation $3.7 \times 10^{-5} \text{ s}^{-1}$.

in the direction of $\nabla\theta$). Frontogenesis is a maximum in a small region of over eastern Maine where the flow is diffluent (Fig. 5b). Southeast of this maxima, frontolysis is diagnosed (Fig. 5c), where the dilatation axes are normal to the isentropes (Fig. 5b).

At 0000 UTC 31 December the cyclonic and anticyclonic upper-tropospheric q'_u are located to the northeast of their positions of 12 h earlier (Fig. 6a). Consistent with the amplification of the anticyclone downstream of the upper trough, we note that the q'_u characterizing the ridge has amplified. The broad southeasterly flow between the anomalies is in a favorable configuration relative to the isentropes to further amplify the lower thermal ridge. South (east) of the positive PV anomaly, along the cold (warm) front, winds are conducive for frontogenesis as the axes of dilatation were parallel to the front (Figs. 6b and 6c). Frontogenesis is again diagnosed northwest of the cyclone center, in the region of diffluent v'_u flow. Moreover, Q'' largely remains parallel to the warm and cold fronts oriented nearly 90° to the left of the temperature gradient along the cold front, and nearly 90° to the

right along the warm front. This configuration of Q'' suggests further amplification of the thermal ridge and intensification of the fronts bounding the thermal ridge (Fig. 6c).

2) FRONTOGENETIC CHARACTERISTICS OF THE MDTROPHOSPHERIC PV ANOMALIES

The q'_m distribution is characterized by patches of relatively small positive and negative anomalies at 0000 UTC 30 December (Fig. 7b). Note that the smallest-scale features in the perturbation PV distribution are not associated with any coherent circulations—indicating that the small-scale PV variations have relatively small influence on the surrounding flow. In the vicinity of the developing warm front, there is a relatively small region of diffluence with dilatation axes of the 925 hPa v'_m flow parallel to the developing warm front between the negative q'_m along the northeast and mid-Atlantic coasts, and the positive q'_m south and east of Newfoundland (Fig. 7a and 7b). Frontogenesis is occurring in this region, as Q'' is oriented parallel to $\nabla\theta$ (Fig. 7c).

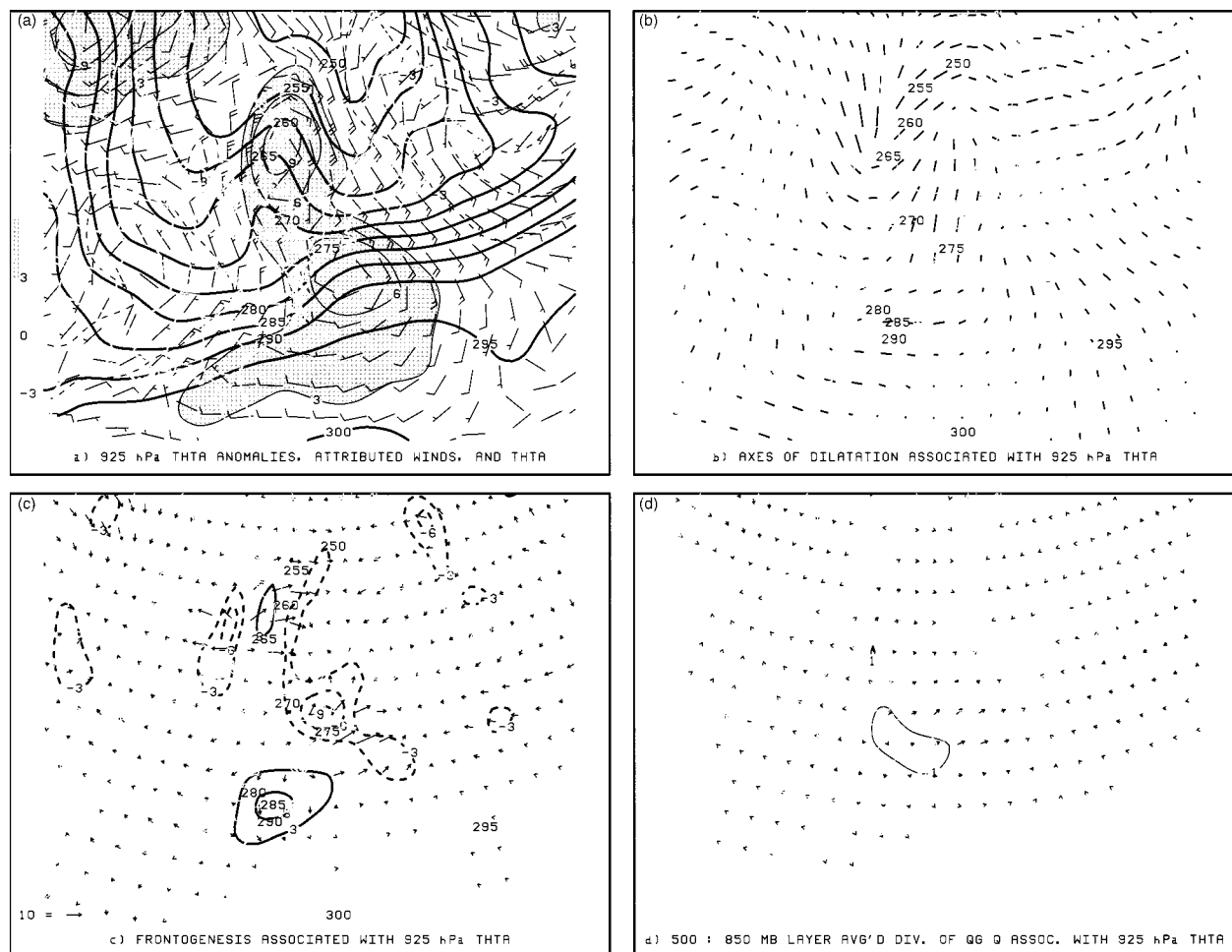


FIG. 10. The 925-hPa potential temperature (solid, heavy contour, interval 5 K) and (a) 925-hPa winds attributed to 925-hPa potential temperature anomalies (contoured and shaded, contour interval 5 K, negative values dashed), (b) 925-hPa axes of dilatation for winds attributed to 925-hPa potential temperature anomalies (maximum deformation $9.1 \times 10^{-5} \text{ s}^{-1}$), (c) 925-hPa balanced \mathbf{Q} vectors and \mathbf{Q} -vector frontogenesis [heavy contoured, negative values dashed, contour interval $3 \text{ K} (1000 \text{ km})^{-1} (3 \text{ h})^{-1}$] attributed to the 925-hPa potential temperature anomalies, and (d) 500–850 hPa-layer-averaged geostrophic \mathbf{Q} vectors and geostrophic \mathbf{Q} -vector convergence (contour, interval $1 \times 10^{-15} \text{ K m}^{-2} \text{ s}^{-1}$) attributed to the 925-hPa potential temperature anomalies for 0000 UTC 30 Dec 1993.

By 1200 UTC 30 December the q'_m (Fig. 8a) are larger in areal extent than in the previous 12 h. A positive anomaly has appeared to the southeast of the New England coast. This anomaly is likely due to an increase in PV due to diabatic processes north of the warm front (recall the reports of heavy snowfall in that region). A larger negative anomaly is found over interior New England. Associated with this anomaly and a larger area of positive q'_m in the southeastern United States (whose existence is related to the increased stratification behind the cold front) is a \mathbf{v}'_m southeast flow extending from the cold front to western New York state. This is a frontolytic situation as seen in Fig. 8b—the axes of dilatation are normal to the front. That $\mathcal{F}^m < 0$ is confirmed as \mathbf{Q}^m points antiparallel to the thermal gradient. Southeast of Nova Scotia, along the developing warm front, \mathbf{Q}^m locally points in the direction of $\nabla\theta$ and hence indicates warm frontogenesis (Fig. 8c).

In the 12 h ending 0000 UTC 31 December, q'_m has undergone further amplification (Fig. 9a). This increase is attributed to latent heat release associated with the precipitation having occurred to the north and northwest of the cyclone. At this time \mathbf{v}'_m is largely frontolytic with the exception of a small region of frontogenesis in the Gulf of Maine where the axes of dilatation are parallel to the isentropes (Fig. 9b). Now \mathbf{Q}^m has also amplified with the largest magnitudes of \mathbf{Q}^m along the warm and cold fronts (Fig. 9c). Also $\mathcal{F}^m < 0$ along both the warm and cold fronts where the circulations around the PV anomaly over the southeastern United States and the PV anomaly over New England are frontolytic (Figs. 9a and 9c). The northwest flow to the west of the diabatically generated cyclonic q'_m , would tend to weaken the 925-hPa thermal ridge. The distribution of \mathbf{Q}^m at this time is consistent with the \mathbf{v}'_m flow tending to weaken the thermal ridge as the components of \mathbf{Q}^m parallel to the isentropes, Q'_s point away from the thermal ridge.

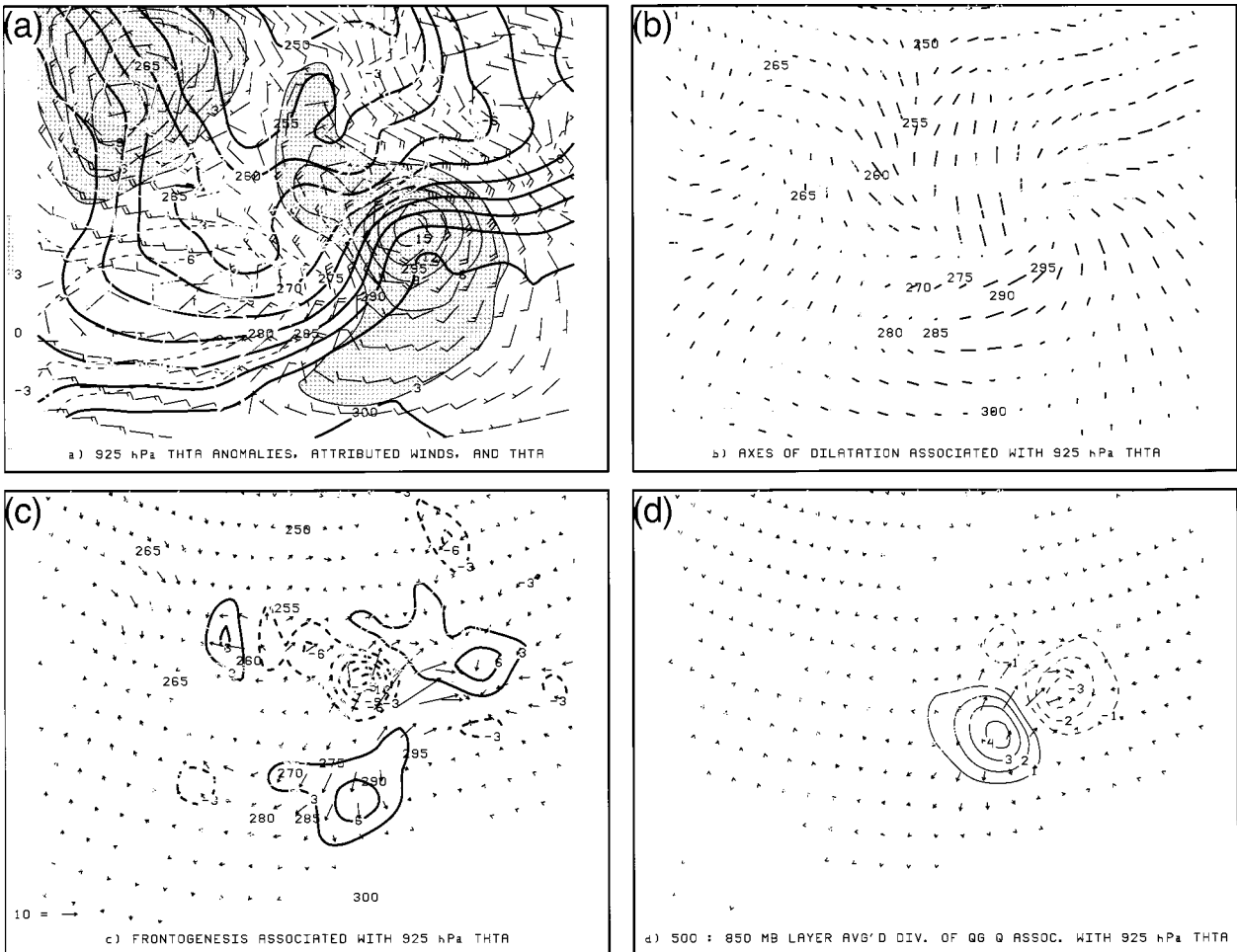


FIG. 11. As in Fig. 10 except for 1200 UTC 30 Dec 1993. Maximum deformation $9.9 \times 10^{-5} \text{ s}^{-1}$.

3) FRONTOGENETIC CHARACTERISTICS OF THE NEAR-SURFACE POTENTIAL TEMPERATURE ANOMALIES

Over eastern North America, there are two maxima in the perturbation potential temperature θ' at 0000 UTC 30 December. One maximum is located over western Quebec, the second along the axis of the thermal ridge east of the mid-Atlantic coast (Fig. 10a). Consistent with the invertibility principle, the wind field (\mathbf{v}'_i) around the warm boundary $\theta' > 0$ is cyclonic. It is apparent that the 925-hPa \mathbf{v}'_i is greater in magnitude than \mathbf{v}'_m and \mathbf{v}'_u . Furthermore it is seen that the shape of the thermal anomalies and PV perturbations have an influence on the shape of the flow field attributed to them. The deformation and cyclonic shear seen in \mathbf{v}'_i along the southeast coast of the United States (Figs. 10a and 10b) are conducive for frontogenesis over the Carolinas and along the southeast coast of Georgia. Consistent with this diagnosis, \mathbf{Q}' is directed from cold to warm (i.e., $\mathcal{F}^I < 0$) along the southeast coast (Fig. 10c). Frontolysis is diagnosed north and east of the 925-hPa thermal ridge where \mathbf{Q}' has components antiparallel to $\nabla\theta$.

To the east-northeast of the thermal ridge, there is a significant component of \mathbf{Q}' along the isentropes, indicating that $\nabla\theta$ should rotate counterclockwise—the isentropes becoming more oriented southwest–northeast. This configuration indicates an amplification of the thermal ridge east-northeast of its current location—implying east-northeastward propagation.

By 1200 UTC 30 December the θ' characterizing the axis of the thermal ridge has amplified by 10 K (Fig. 11a) and the ridge has propagated east-northeastward. The broad negative thermal anomaly over the southern United States is associated with the colder than the 5-day time-mean air advected southward in the wake deepening cyclone. Between this anomaly and the positive θ' associated with the axis of the thermal ridge is \mathbf{v}'_i flow with axes of dilatation along the cold front (Fig. 11b). Consonant with this configuration of isentropes and axes of dilatation, frontogenesis along the cold front is diagnosed (Fig. 11c). Warm frontogenesis is also diagnosed east of the thermal ridge axis.

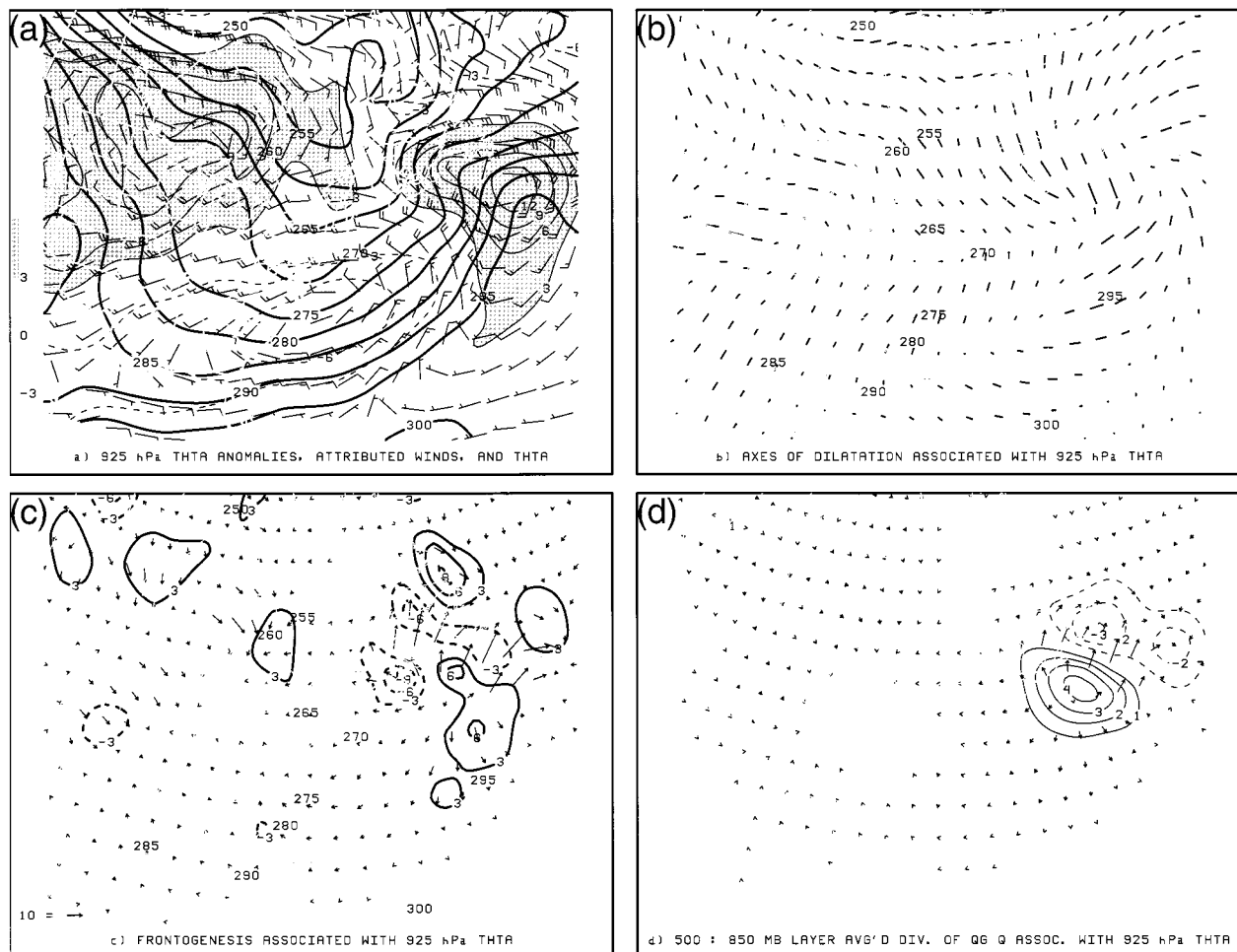


FIG. 12. As in Fig. 10 except for 0000 UTC 31 Dec 1993. Maximum deformation $8.8 \times 10^{-5} \text{ s}^{-1}$.

The diffluent flow between the θ' characterizing the 925-hPa thermal ridge and the cold θ' to the southwest of that ridge continue to support cold frontogenesis at 0000 UTC 31 December (Figs. 12a and 12b). Along and to the north of the axis of the thermal ridge, \mathbf{v}'_i is frontolytic. Confluent frontogenesis is diagnosed along the warm front where the axes of dilatation are parallel to the isentropes. The \mathbf{Q}' vectors confirm this qualitative diagnosis as $\mathcal{F}' > 0$ along the warm and cold fronts while $\mathcal{F}' < 0$ is diagnosed in the thermal ridge axes. The distribution of \mathbf{Q}' is "patchy" and the magnitudes of the vectors generally small except along the warm front (Fig. 11c).

4) FRONTOGENETIC CHARACTERISTICS OF THE IRRATIONAL FLOW

Figure 13a shows \mathbf{v}_x superposed on analyses of 925-hPa divergence and potential temperature. Convergence is observed along the baroclinic zones flanking the thermal ridge. Along the Virginia, Maryland, Del-

aware, and North Carolina coasts, along the cold side of the developing cold front, frontogenesis is diagnosed as the axis of dilatation of the irrotational flow is parallel to the isentropes and where the flow is convergent (Figs. 13a and 13b). On the cold side of the developing warm front, frontogenesis is also diagnosed as the deformation pattern associated with \mathbf{v}_x is both confluent and convergent in that region (Figs. 13b and 13c). At this and later times, \mathbf{Q}^x is characterized by a relatively large component perpendicular to the isentropes.

At 1200 UTC 30 December, convergence along the warm front and a favorable orientation of the dilatation axes associated with \mathbf{v}_x indicates frontogenesis along the warm front (Figs. 14a and 14b). A decreasing front-normal component of \mathbf{v}_x (diffluence) flowing toward the warm air behind the advancing cold front suggests frontogenesis along the cold front as well (Fig. 14a). Note that \mathcal{F}^x shows a propensity to be maximized along the warm front at 1200 UTC 30 December (Fig. 14c).

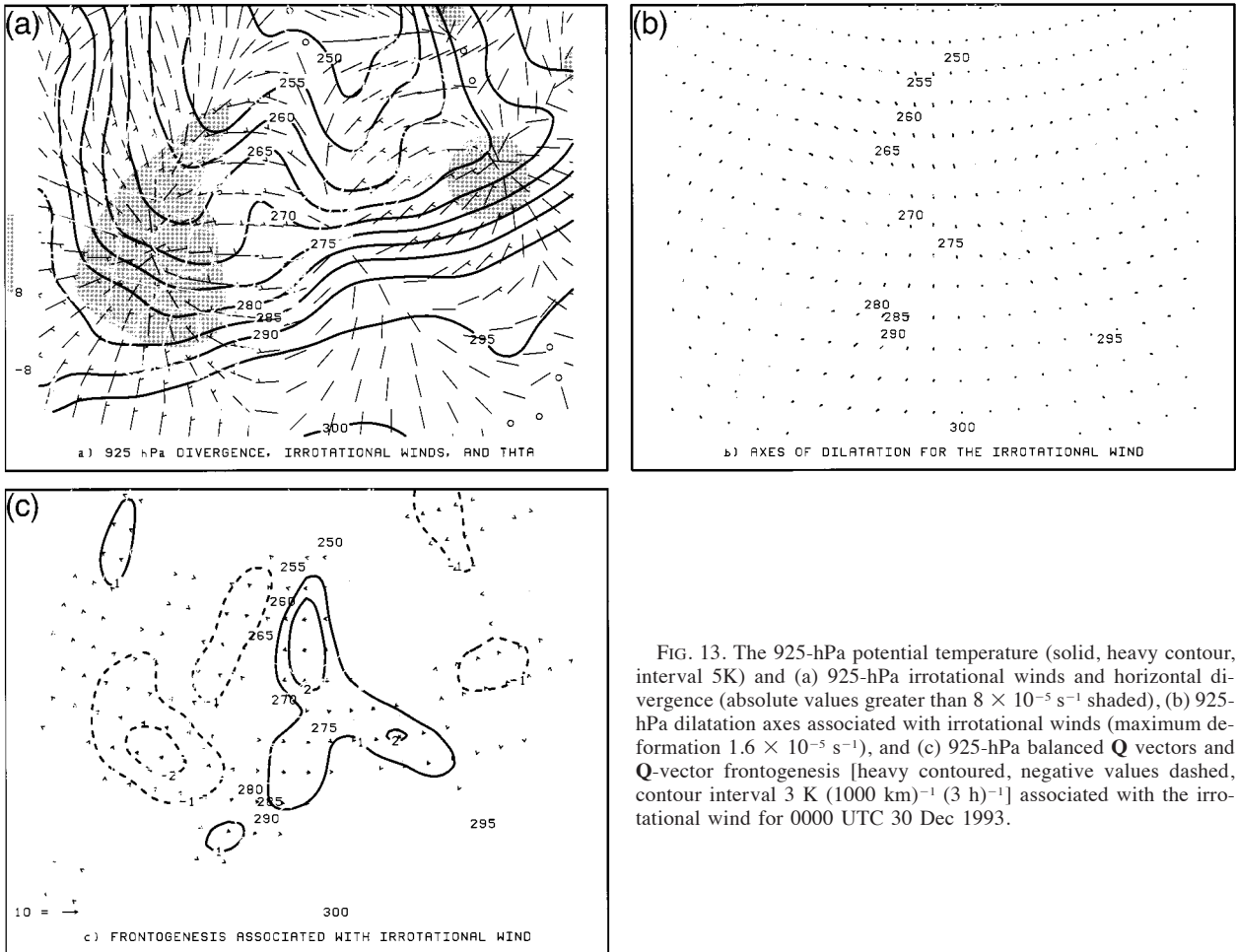


FIG. 13. The 925-hPa potential temperature (solid, heavy contour, interval 5K) and (a) 925-hPa irrotational winds and horizontal divergence (absolute values greater than $8 \times 10^{-5} \text{ s}^{-1}$ shaded), (b) 925-hPa dilatation axes associated with irrotational winds (maximum deformation $1.6 \times 10^{-5} \text{ s}^{-1}$), and (c) 925-hPa balanced \mathbf{Q} vectors and \mathbf{Q} -vector frontogenesis [heavy contoured, negative values dashed, contour interval 3 K (1000 km) $^{-1}$ (3 h) $^{-1}$] associated with the irrotational wind for 0000 UTC 30 Dec 1993.

By 0000 UTC 31 December, the divergence is a local maximum east of the New Jersey coast and is a local minimum (convergence) to the east of St. John's, Newfoundland (Fig. 15a). Between these two extrema, \mathbf{v}_χ reaches a maximum magnitude and this configuration is frontolytic to the south and west of the thermal ridge. Also, \mathbf{v}_χ is frontogenetic along the warm front (Fig. 15a) where the flow is convergent and frontogenetic along the cold front where \mathbf{v}_χ is diffluent but not convergent (Figs. 15b and 15c).

5. Diagnosing vertical motion using the partitioned geostrophic Q-vector divergence

Within the context of QG dynamics, the proposed partitioning of the geostrophic \mathbf{Q} vector, \mathbf{Q}_g , allows for the direct attribution of vertical motion to individual PV anomalies:

$$L(\omega) = -2\nabla \cdot \mathbf{Q}_g$$

$$= -2(\nabla \cdot \mathbf{Q}_g^u + \nabla \cdot \mathbf{Q}_g^m + \nabla \cdot \mathbf{Q}_g^l + \nabla \cdot \mathbf{Q}_g^{\text{mean}}).$$

The contributions, ω_k , to the diagnosed vertical motion, ω , are given by solutions to

$$L(\omega_k) = -2\nabla \cdot \mathbf{Q}_g^k \tag{5.1}$$

with boundary conditions imposed.⁴ In this section we discuss the distribution of $\nabla \cdot \mathbf{Q}_g^k$ averaged over a deep layer from 850 to 500 hPa shown in panel d of Figs. 4–6 for the upper PV anomaly, Figs. 7–9 for the middle and lower-tropospheric PV anomaly, and Figs. 10–12 for the lower boundary potential temperature. As noted earlier, the divergence of the \mathbf{Q}_g vector through a sufficiently deep layer is a diagnostic of vertical motion, with ascent (descent) associated with \mathbf{Q}_g -vector convergence (divergence).

⁴ An alternate assessment of the vertical motion associated with individual PV anomalies is presented by Davis (1992b): The prognostic balance system is first solved for ω_{full} associated with the full PV distribution and solved again for ω_{alt} associated with a distribution of PV for which the PV perturbation of interest has been removed. The difference, $\omega_{\text{full}} - \omega_{\text{alt}}$, is the vertical motion field associated with the PV anomaly of interest.

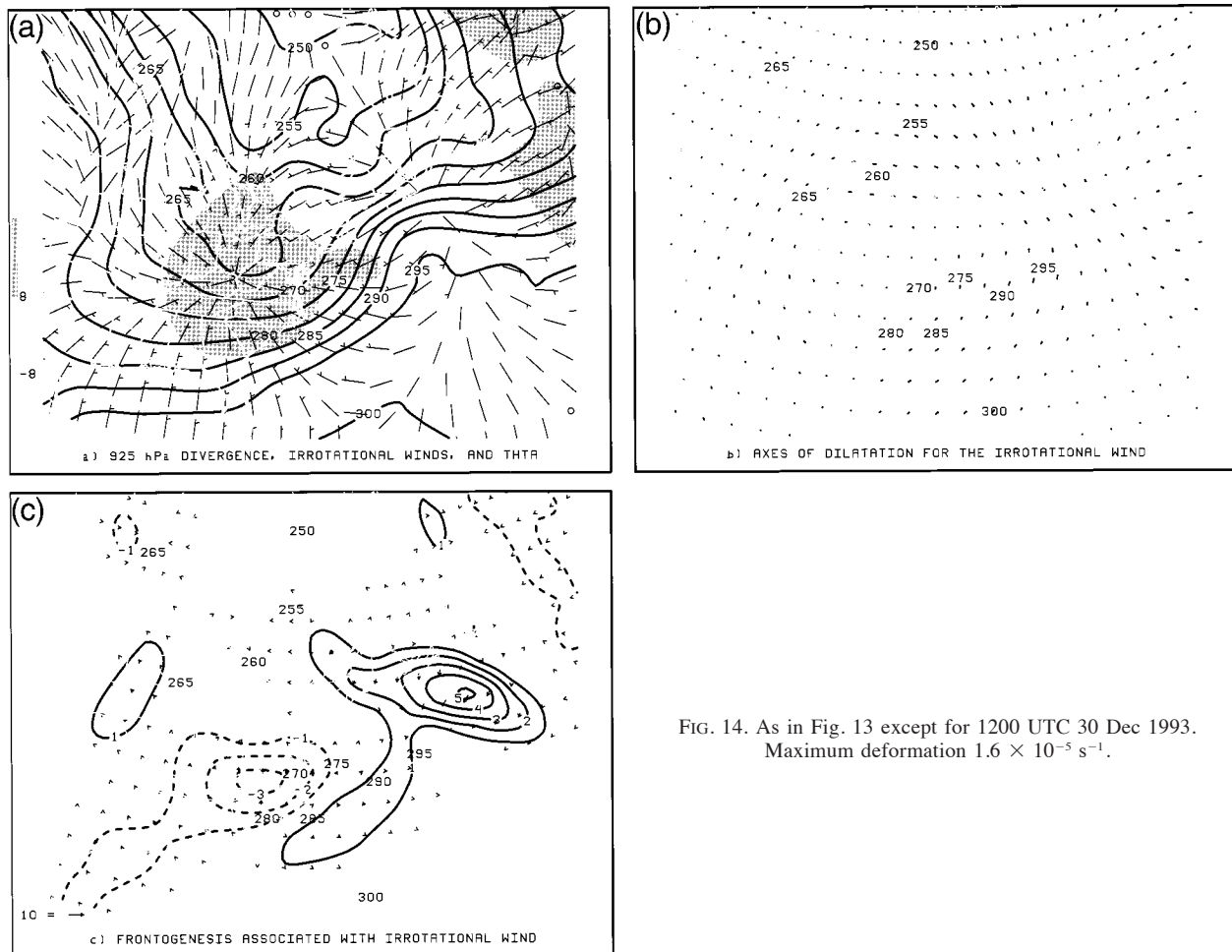


FIG. 14. As in Fig. 13 except for 1200 UTC 30 Dec 1993. Maximum deformation $1.6 \times 10^{-5} \text{ s}^{-1}$.

a. Forcing for vertical motion attributed to the upper-tropospheric PV

Associated with the upper trough, at all times, is a positive–negative couplet of $\nabla \cdot \mathbf{Q}_g^u$ straddling the upper trough axis. Such a configuration is consistent with the anticipated ascent (descent) diagnosed downstream (upstream) of the trough axis (Figs. 4d, 5d, and 6d). We note that the pattern of \mathbf{Q}_g^u at 1200 UTC 30 December and 0000 UTC 31 December is most like the pattern of 925 hPa \mathbf{Q}^u . It is at these two times that $\mathbf{v}'_{g,u}$ is most in phase with the amplifying thermal ridge.

b. Forcing for vertical motion attributed to the middle and lower-tropospheric PV

Because the distribution of \mathbf{Q}_g^m at 0000 UTC 30 December is characterized by vectors of small magnitude and no coherent patterns of orientation, $\nabla \cdot \mathbf{Q}_g^m$ is also small (Fig. 7d), and, as a consequence, one may conclude that vertical motions in the lower troposphere associated with the PV anomalies in the middle and lower-troposphere are small. As the PV anomalies in the lower

troposphere have begun to amplify by 1200 UTC 30 December, the forcing for vertical motion also amplifies. Alternating regions of convergence and divergence of \mathbf{Q}_g^m extending from the mid-Atlantic coast to southeast of Nova Scotia describe the distribution at this time. (Fig. 9c). By 0000 UTC 31 December the contribution to the vertical motion due to the middle and lower-tropospheric PV is at its greatest amplitude for the three times described. At this time, $\nabla \cdot \mathbf{Q}_g^m$ is characterized by relative large-scale, coherent bands of forcing for ascent and descent extending approximately 600 km southeast from eastern Newfoundland and southeast from the Gulf of Maine (Fig. 9d).

c. Forcing for vertical motion attributed to the lower-tropospheric PV

At 0000 UTC 30 December the distributions of both \mathbf{Q}_g^l and $\nabla \cdot \mathbf{Q}_g^l$ are small in magnitude (Fig. 10d). The largest values of $\nabla \cdot \mathbf{Q}_g^l$ are found in a band extending southeastward from northeastern Ohio to southeastern Maryland. Twelve hours later (Fig. 11d), when the am-

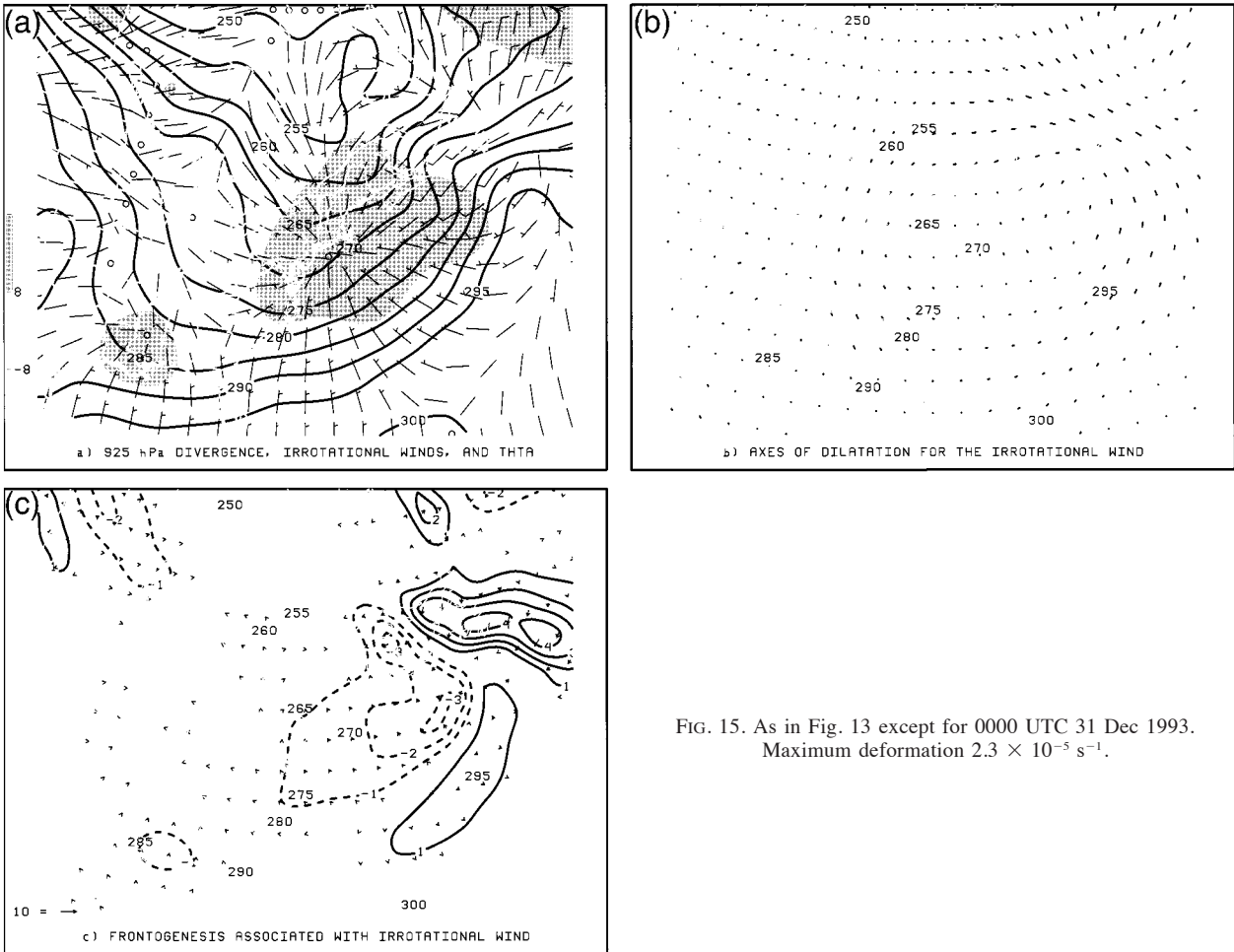


FIG. 15. As in Fig. 13 except for 0000 UTC 31 Dec 1993. Maximum deformation $2.3 \times 10^{-5} \text{ s}^{-1}$.

plitude of the thermal anomaly characterizing the thermal ridge has increased to 16 K, the magnitudes of both \mathbf{Q}'_g and $\nabla \cdot \mathbf{Q}'_g$ are also large. The distribution of the inferred vertical motion is congruous with the pattern of vertical motion one might expect with a propagating lower edge wave—ascend ahead of the thermal ridge, descent behind. By 0000 UTC 31 December this distribution remains the essentially the same except the pattern is now located to the east-northeast of its 1200 UTC 30 December position (Fig. 12d).

6. Summary

For a given surface potential temperature gradient, the vector surface frontogenesis (changes in the magnitude and orientation of the potential temperature gradient) associated with the surface wind field is dependent on the deformation, divergence, and vorticity of the surface wind. The surface wind field and its associated kinematic properties at any arbitrary location may be viewed as the net effect of contributions to the wind field attributed to local and remote PV anomalies. In this paper, we have presented a technique for diagnosing

the contributions of PV anomalies to the vector frontogenesis through the use of a piecewise PV partitioning of the \mathbf{Q} vector framed in the context of the nonlinear balanced dynamics. In addition, we have used the partitioned geostrophic \mathbf{Q} vectors to diagnose the distributions of forcing for vertical motion attributed to particular portions of the perturbation PV.

a. Summary of results

1) FRONTOGENETIC CHARACTERISTICS OF THE TOTAL PERTURBATION FLOW

Figure 16 shows the distribution of the total perturbation \mathbf{Q} vector, \mathbf{Q}' ,

$$\mathbf{Q}' = \mathbf{Q}'' + \mathbf{Q}^m + \mathbf{Q}^l + \mathbf{Q}^x,$$

(the sum of the portions of the balanced perturbation \mathbf{Q} vectors and the \mathbf{Q} vectors associated with the irrotational wind), and $\mathcal{F}' = \mathbf{Q}' \cdot \nabla \theta$, for 0000 UTC 30 December–0000 UTC 31 December. At all times, \mathbf{Q}' is dominated by the contributions of \mathbf{Q}'' and \mathbf{Q}^l . The relative contributions to \mathcal{F}' from the four components

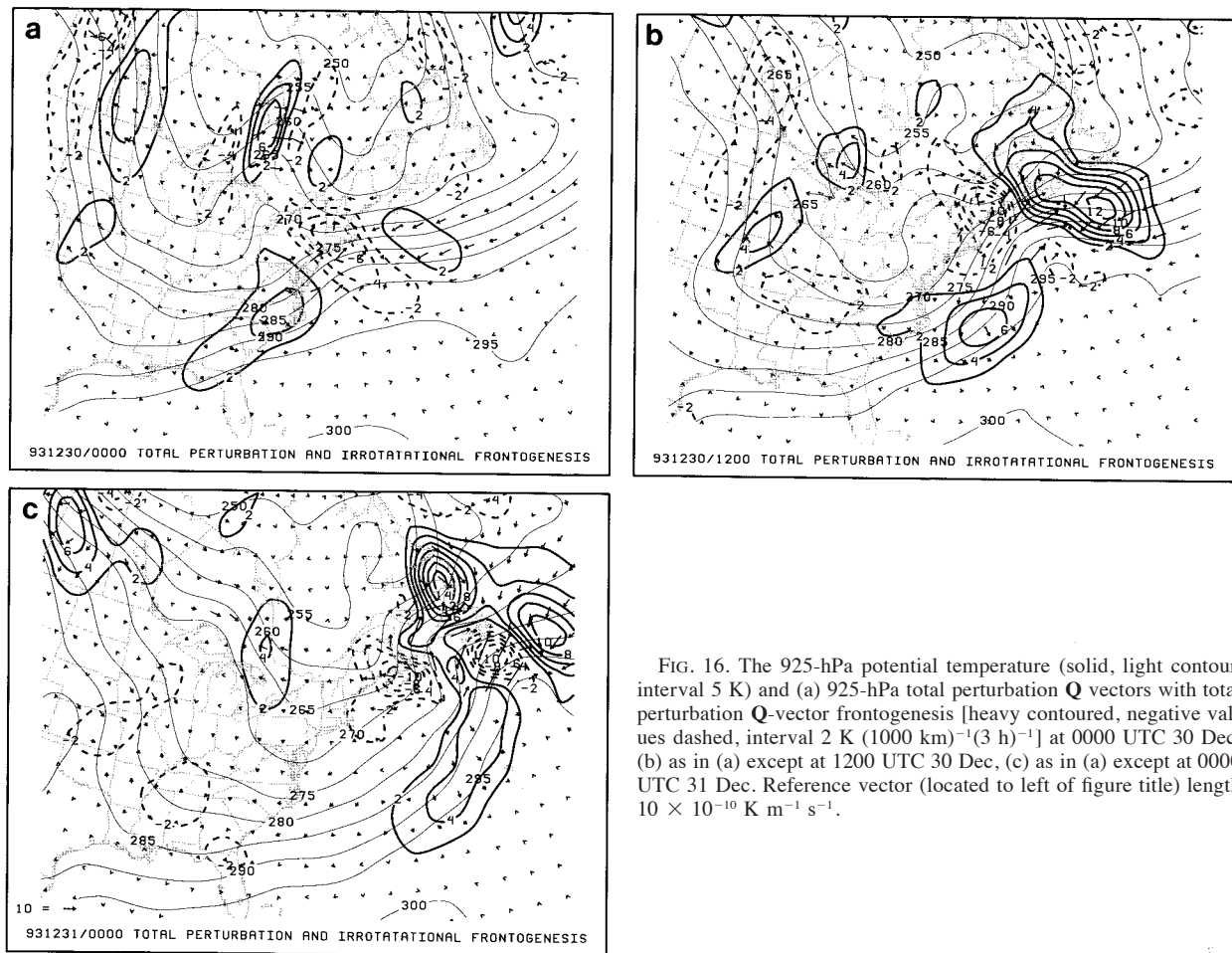


FIG. 16. The 925-hPa potential temperature (solid, light contour, interval 5 K) and (a) 925-hPa total perturbation \mathbf{Q} vectors with total perturbation \mathbf{Q} -vector frontogenesis [heavy contoured, negative values dashed, interval 2 K (1000 km) $^{-1}$ (3 h) $^{-1}$] at 0000 UTC 30 Dec, (b) as in (a) except at 1200 UTC 30 Dec, (c) as in (a) except at 0000 UTC 31 Dec. Reference vector (located to left of figure title) length 10×10^{-10} K m $^{-1}$ s $^{-1}$.

change with respect to location and with respect to time. While along the cold front \mathcal{F}^l and \mathcal{F}^x positively contribute to frontogenesis for all times, \mathcal{F}^x is a consistent contributor to frontogenesis along the warm front. The flow associated with the upper-tropospheric PV anomaly, \mathbf{v}'_u , contributes to frontolysis along the cold front at the early stages of the cyclogenesis event, while at later times \mathbf{v}'_u contributes to frontogenesis along the cold front.

The contributions to the middle tropospheric PV anomalies during the evolution of this cyclone are generally small and vary widely with respect to location and magnitude and sign. No coherent signal is evident in this particular case.

Along the axis of the thermal ridge, \mathcal{F}^l and \mathcal{F}^u yield a consistent negative contribution to \mathcal{F}^l . This distribution of frontogenesis results in a region of frontolysis separating the regions of frontogenesis along the warm and cold fronts. It is possible that this "fracture" in the frontogenesis distribution is related to the phenomenon of frontal fracture: a loss of cold frontal baroclinicity near the cyclone center during the early stages in a baroclinic waves' life cycle (e.g., Hoskins 1976; Hos-

kins and West 1979; Shapiro and Keyser 1990; Rotunno et al. 1994). While the data available in the current study is incapable of resolving a frontal fracture, preliminary results of numerical simulations of this cyclone event indicate that a fracture did form—suggesting the diagnostic calculations presented were identifying an important frontal process. Applying this technique to other cyclone events, should shed light on the important mechanisms for frontal fracture.

This study was limited to the diagnosis of near-surface frontogenesis associated with the quasi-horizontal portion of the flow. Near the earth's surface, over flat topography, the neglect of the vertical motion contribution to frontogenesis is not too serious as the vertical motion in such regions is generally small. If one were interested in applying these techniques to midtropospheric frontogenesis, in principle, the frontogenesis associated with the vertical component of the divergent circulation (i.e., the vertical velocity) obtained from a solution to the balance system could be calculated using the three-dimensional frontogenesis function (Miller 1948).

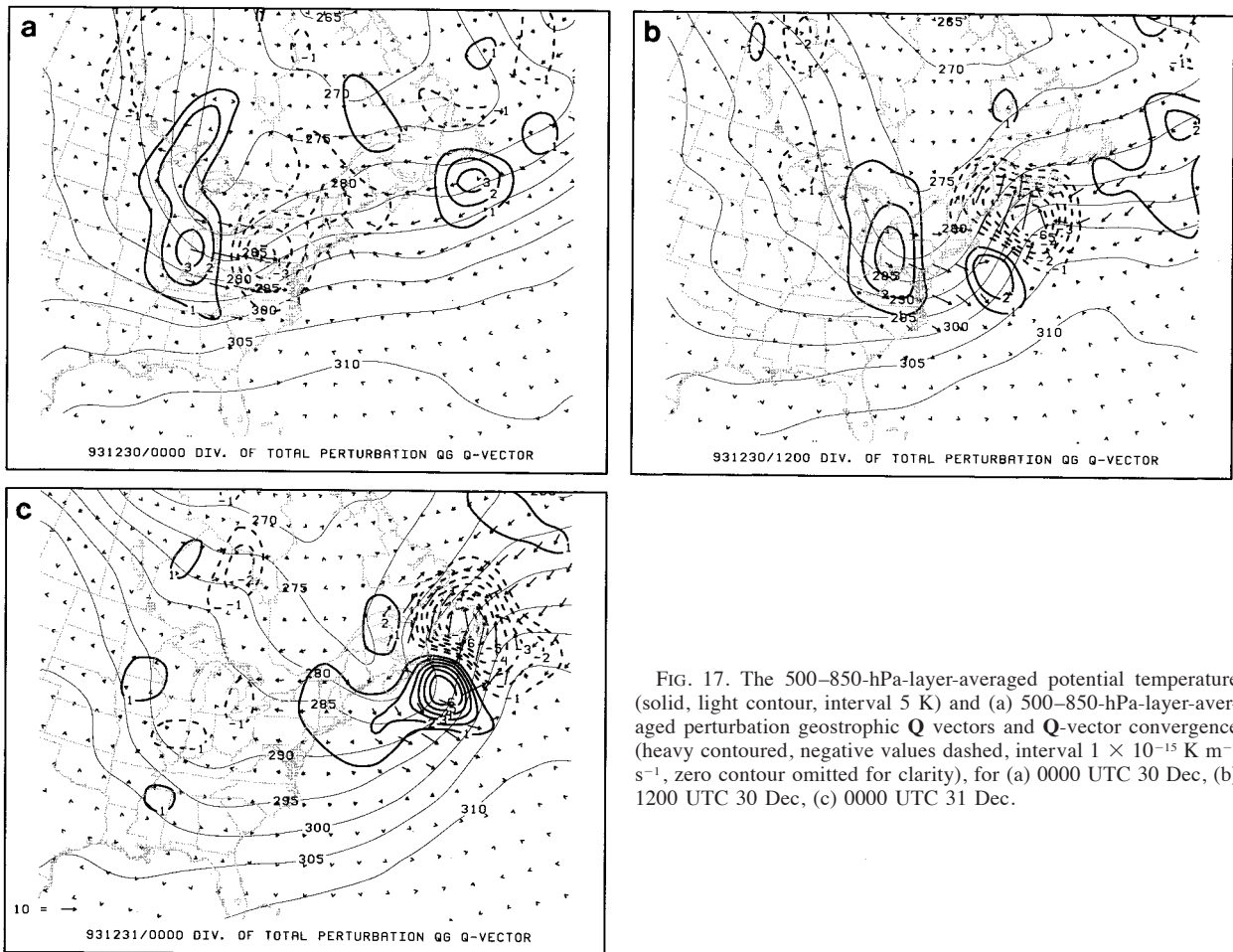


FIG. 17. The 500–850-hPa-layer-averaged potential temperature (solid, light contour, interval 5 K) and (a) 500–850-hPa-layer-averaged perturbation geostrophic \mathbf{Q} vectors and \mathbf{Q} -vector convergence (heavy contoured, negative values dashed, interval $1 \times 10^{-15} \text{ K m}^{-2} \text{ s}^{-1}$, zero contour omitted for clarity), for (a) 0000 UTC 30 Dec, (b) 1200 UTC 30 Dec, (c) 0000 UTC 31 Dec.

2) TOTAL PERTURBATION FORCING FOR VERTICAL MOTION

Figure 17 shows the distribution of the sum of the contributions to $\nabla \cdot \mathbf{Q}_g$ from the upper-PV anomalies, middle- and lower-tropospheric anomalies, and near-surface potential temperature anomalies superposed on the layer mean potential temperature distribution for each of the three times discussed earlier in the text. For this case, the two dominant contributors to vertical motion were the upper-tropospheric PV anomalies and the near-surface thermal perturbations. Here $\nabla \cdot \mathbf{Q}_g^u$ constitutes most of the forcing at the initial time (cf. Figs. 4a, 10a, and 17a) and has a slightly larger contribution than $\nabla \cdot \mathbf{Q}_g^l$ at later times. Slight phase differences exist between $\nabla \cdot \mathbf{Q}_g^u$ and $\nabla \cdot \mathbf{Q}_g^l$ at 1200 UTC 30 December and 0000 UTC 31 December: $\nabla \cdot \mathbf{Q}_g^u$ is negative in the lower-tropospheric ridge, while $\nabla \cdot \mathbf{Q}_g^l$ is negative (positive) northeast (southwest) of the thermal ridge. Dynamically such phase differences suggests that the upper trough is serving to intensify the surface cyclone while the patterns of ascent and descent associated with the lower

thermal perturbation are serving to propagate the cyclone northeastward.

b. Synoptic conceptualizations

While it is improper to generalize the results of a single case to all extratropical cyclones, we believe a few characteristic \mathbf{Q} -vector signatures of synoptic features have been identified that have also been documented in previous observational and theoretical cyclone studies. Furthermore, while this particular case was characterized by rapid deepening, we regard the cyclogenesis event as a “typical event” (an upper trough interacting with a lower tropospheric baroclinic zone) characterized by a vigorous precursor disturbance. The robustness of precursor disturbance and subsequent development of the well-defined thermal ridge provide for clearer resolution of the important factors responsible for the resultant frontogenesis. We relate these \mathbf{Q} -vector signatures to these previously identified structures and summarize the signatures in a series of schematics for idealized examples below.

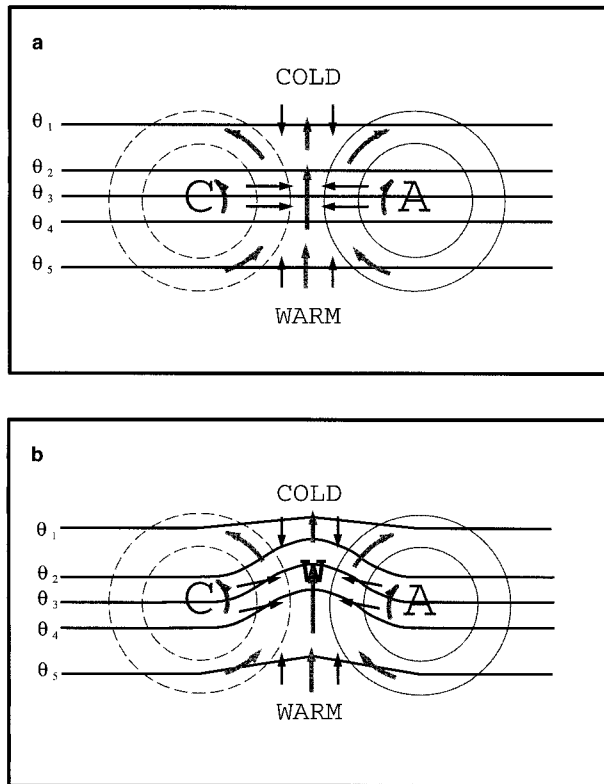


FIG. 18. Schematic of upper trough-ridge pattern interacting with lower-tropospheric baroclinic zone: (a) lower-tropospheric isentropes (solid, dark contours), geopotential height perturbations associated with upper trough-ridge pattern (gray contours, negative values dashed), geostrophic wind vectors (gray arrows) and associated \mathbf{Q} vectors, and \mathbf{Q}_g^u (thin, dark arrows) at some initial time, t_0 ; (b) at some short time later, $t > t_0$. Here C (A) indicates the center of the cyclonic (anticyclonic) circulation associated with the upper-tropospheric positive (negative) PV anomaly.

1) UPPER PV ANOMALIES INTERACTING WITH A BAROCLINIC ZONE

Consider the case of the circulation attributed to a PV dipole interacting with lower-level baroclinic zone (Fig. 18). If the cyclonic (C) and anticyclonic (A) circulations are of the same magnitude, the circulations are associated with strong southerly geostrophic flow maximized halfway between the two anomalies. The flow is weaker near the anomalies and weak to the north and south. The geostrophic \mathbf{Q} vectors for such a flow may be determined with the aid of the technique suggested by Sanders and Hoskins (1990) to estimate the direction and magnitude of \mathbf{Q} vectors: “[In the Northern Hemisphere] the \mathbf{Q} vector can be obtained by traveling along an [isentrope] with the cold air to the left and noting the vector change of the geostrophic wind. Rotating this vector change 90° clockwise gives the direction of the \mathbf{Q} vector. Its magnitude is proportional to the magnitude of the vector rate of change multiplied by the strength of the [potential] temperature gradient.” Applying this rule we obtain the \mathbf{Q} -vector distribution

shown in Fig. 17a. Based on the orientation of \mathbf{Q}_g^u , one would diagnose frontogenesis north of the frontal zone, frontolysis to the south, and a rotation of the potential temperature gradient vector consistent with an amplification of the thermal ridge. The distribution of \mathbf{Q}_g would suggest ascent within the thermal ridge as $\nabla \cdot \mathbf{Q}_g^u < 0$. If the cyclone-anticyclone pair were to continue to amplify the thermal ridge, the distribution of \mathbf{Q} vectors and potential temperature would resemble Fig. 18b. This pattern is quite similar to Fig. 5c. Because $\nabla \cdot \mathbf{Q}_g^u < 0$ within the thermal ridge, ascent is still diagnosed in the narrowing warm sector.

The region of ascent in the thermal ridge is consistent with ascent being diagnosed downstream of an upper trough wherein ascent is found in regions of positive advection of absolute geostrophic vorticity by the thermal wind. From a PV perspective, the creation of a lower boundary thermal ridge implies pressure falls and a concomitant spinup of vorticity at the surface [e.g., Hoskins et al. (1985) Fig. 21 and accompanying discussion]. This spinup of vorticity can be accomplished only through vortex tube stretching—implying ascent in the lower-tropospheric thermal ridge.

The pattern of \mathbf{Q} vectors and the evolving distribution of isentropes shown in Fig. 18 is consistent with the pattern of ascent and evolving thermal structure documented in Martin (1999) as the *trowal* (trough of warm air aloft) of occluding cyclones. In the occluded cyclones studied, Martin determined that the geostrophic contribution to the formation of the thermal ridge is accomplished by \mathbf{Q}_s (the “rotational” \mathbf{Q} vector). Indeed, in this case study, most of the forcing for ascent in the thermal ridge is related to $\mathbf{Q}_{g,s}^u$, that part of \mathbf{Q}_s associated with the upper-tropospheric PV anomaly. Figure 19 shows the distribution of \mathbf{Q}_g^u , $\mathbf{Q}_{g,n}^u$, and $\mathbf{Q}_{g,s}^u$, on the 850-hPa isobaric surface at 1200 UTC 30 December. It is apparent that $\nabla \cdot \mathbf{Q}_g^u$ is dominated by the contribution from $\nabla \cdot \mathbf{Q}_{g,s}^u$. Further, the pattern of vertical motion that might be inferred from $\nabla \cdot \mathbf{Q}_{g,s}^u$ is on the scale of the baroclinic wave, while the pattern of vertical motion that might be inferred from $\nabla \cdot \mathbf{Q}_{g,n}^u$ is frontal scale—an observation consistent with the suggestion of Keyser et al. (1988) and later confirmed by Keyser et al. (1992). The results of this study suggest that the upward motion in lower-tropospheric thermal ridges being amplified by upper troughs may be largely associated with the wind field attributed to the upper trough interacting with the lower-tropospheric baroclinic zone.

2) FRONTOGENESIS AND VERTICAL MOTION ATTRIBUTED TO A SURFACE EDGE WAVE

We consider an idealized thermal ridge similar to the thermal perturbation seen in Fig. 11a. To the distribution of lower boundary, θ' may be attributed a distribution of geostrophic winds, and \mathbf{Q}_g^l shown in Fig. 20. The pattern of \mathbf{Q}_g^l relative to $\nabla\theta$ implies $\mathcal{F}^l > 0$ in the northeast and southwest quadrants, while $\mathcal{F}^l < 0$ in the north-

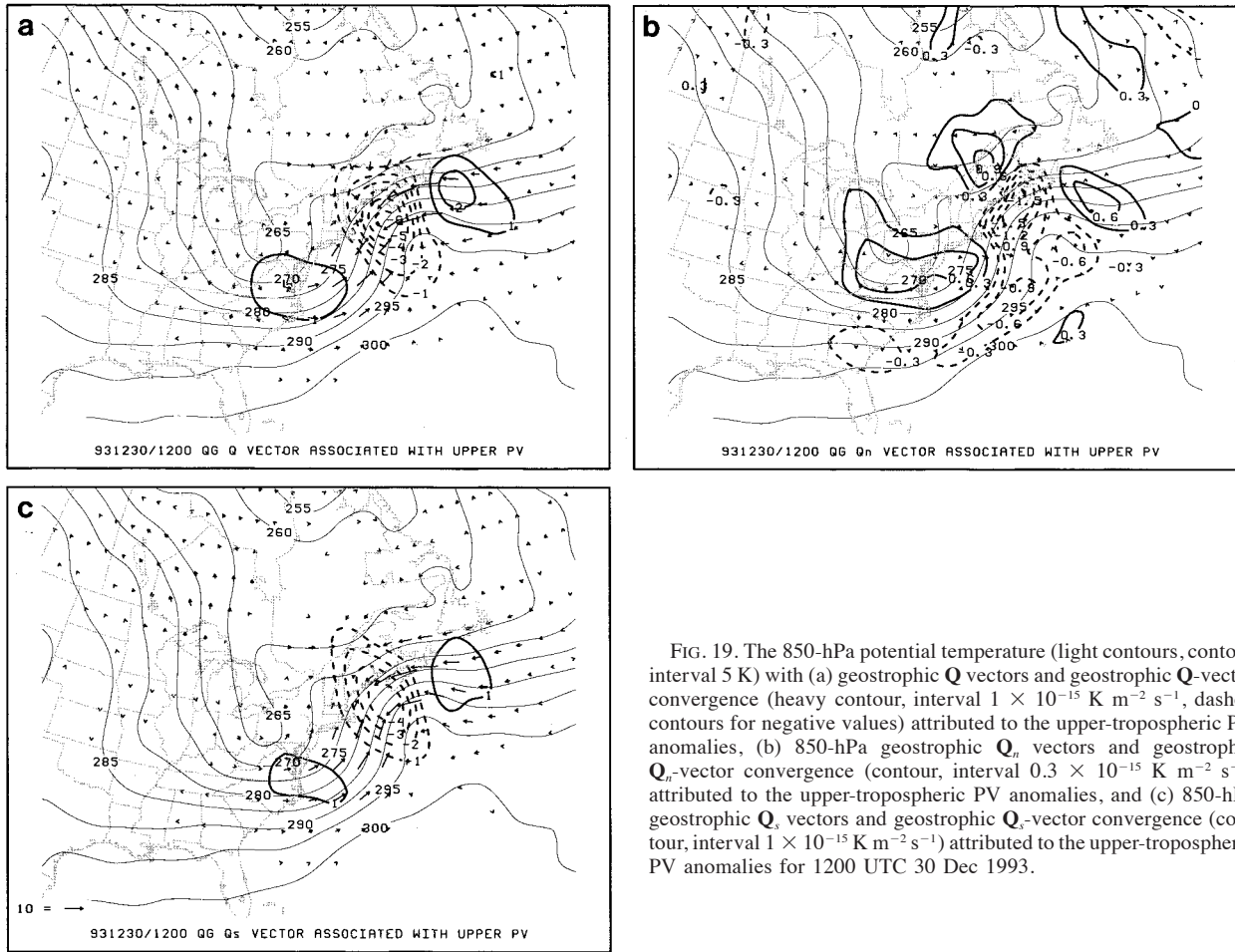


FIG. 19. The 850-hPa potential temperature (light contours, contour interval 5 K) with (a) geostrophic \mathbf{Q} vectors and geostrophic \mathbf{Q} -vector convergence (heavy contour, interval $1 \times 10^{-15} \text{ K m}^{-2} \text{ s}^{-1}$, dashed contours for negative values) attributed to the upper-tropospheric PV anomalies, (b) 850-hPa geostrophic \mathbf{Q}_n vectors and geostrophic \mathbf{Q}_n -vector convergence (contour, interval $0.3 \times 10^{-15} \text{ K m}^{-2} \text{ s}^{-1}$) attributed to the upper-tropospheric PV anomalies, and (c) 850-hPa geostrophic \mathbf{Q}_s vectors and geostrophic \mathbf{Q}_s -vector convergence (contour, interval $1 \times 10^{-15} \text{ K m}^{-2} \text{ s}^{-1}$) attributed to the upper-tropospheric PV anomalies for 1200 UTC 30 Dec 1993.

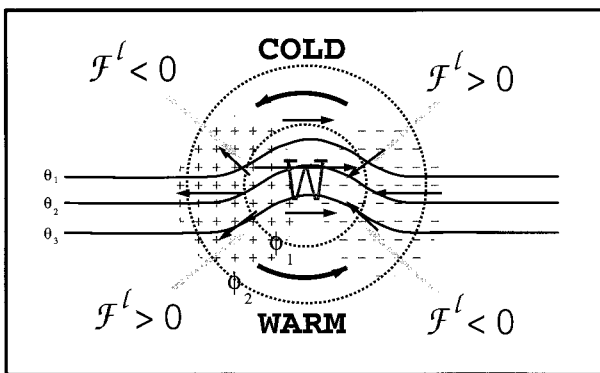


FIG. 20. Schematic of lower-tropospheric thermal wave pattern: lower-tropospheric isentropes (solid, dark contours), geopotential height perturbations associated with thermal ridge (short dashed contours; labeled φ_1 and φ_2 , with $\varphi_1 < \varphi_2$), geostrophic wind vectors (curved arrows), and associated \mathbf{Q} vectors (thin, dark arrows). Here, W indicates the location of the maximum warm anomaly. Regions of frontogenesis ($\mathcal{F}^l > 0$) and frontolysis ($\mathcal{F}^l < 0$) are indicated. Areas of \mathbf{Q} vector divergence and convergence are indicated by the $+$'s and $-$'s respectively.

west and southeast quadrants. The distribution of \mathbf{Q}'_g is characterized by $\nabla \cdot \mathbf{Q}'_g < 0$ ahead of the thermal ridge and $\nabla \cdot \mathbf{Q}'_g > 0$ behind the ridge. This figure may be compared with Figs. 11c and 11d.

As noted in the previous section, the disturbance discussed here is an Eady edge wave: a neutral, surface-trapped baroclinic wave in a semi-infinite, uniform PV, quasigeostrophic fluid. Such waves propagate eastward relative to the surface flow in the presence of a southward-directed surface potential temperature gradient (e.g., Gill 1992). While at any instant in time frontogenesis is occurring along the cold front and frontolysis is occurring along the warm front, this frontogenesis is transient.

3) FRONTOGENESIS ASSOCIATED WITH THE IRROTATIONAL WIND

Throughout the development of the extratropical cyclone described in section 4, \mathbf{v}_x was frontogenetical along both the warm and cold fronts. A common feature

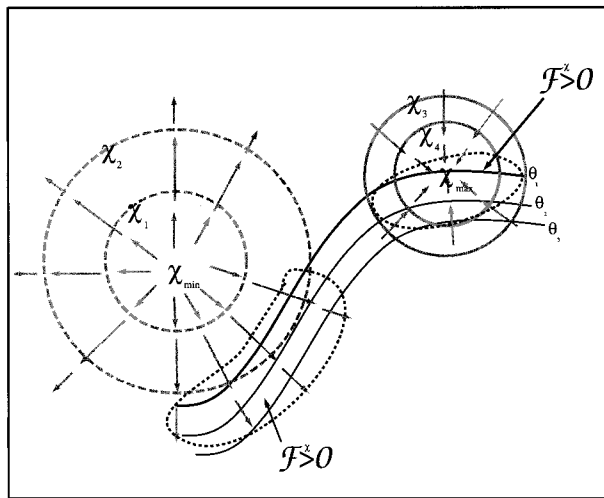


FIG. 21. Schematic of the effects of the irrotational wind on the lower-tropospheric potential temperature distribution during an extratropical cyclogenesis event. Shown are lower-tropospheric isentropes (solid, dark contours), velocity potential associated with thermal ridge (gray contours; negative contours dashed labeled $\chi_1, \chi_2, \chi_3, \chi_4$, with $\chi_1 < \chi_2 < \chi_3 < \chi_4$), irrotational wind vectors (gray arrows), and regions of frontogenesis associated with the irrotational wind. Extrema in velocity potential labeled.

of Figs. 13, 14, and 15 (and likely of most propagating extratropical cyclones) is the location of the maximum convergence (maximum χ) ahead of the cyclone (near the warm front), and the maximum divergence (minimum χ) behind the cyclone (in the cold air). For this particular cyclone, the maximum convergence was located over the warm front and hence was frontogenetical [recall (2.1)]. The maximum divergence was located southwest of the cyclone, behind the cold front. Given the structure of the velocity potential and the position of the cold front relative to the maximum in χ , ∇_{χ} was characterized by diffluent flow along the cold frontal zone with axes of dilatation parallel to the front. Figure 21 summarizes the configuration of isentropes, velocity potential extrema, ∇_{χ} , and the associated regions of frontogenesis.

4) FRONTGENESIS ASSOCIATED WITH SPATIAL INHOMOGENEITIES IN STRATIFICATION

The effects of horizontal variations stratification may play an important role in the frontogenesis associated with upper-tropospheric PV anomalies. Recall that the effective depth of influence of a PV anomaly, h , varies as

$$h \sim \frac{fL}{N}$$

As a consequence, for a PV anomaly of a given horizontal scale, L , at a particular latitude, the depth of influence of the anomaly will be greatest where the reference state stratification (N , the Brunt-Väisälä fre-

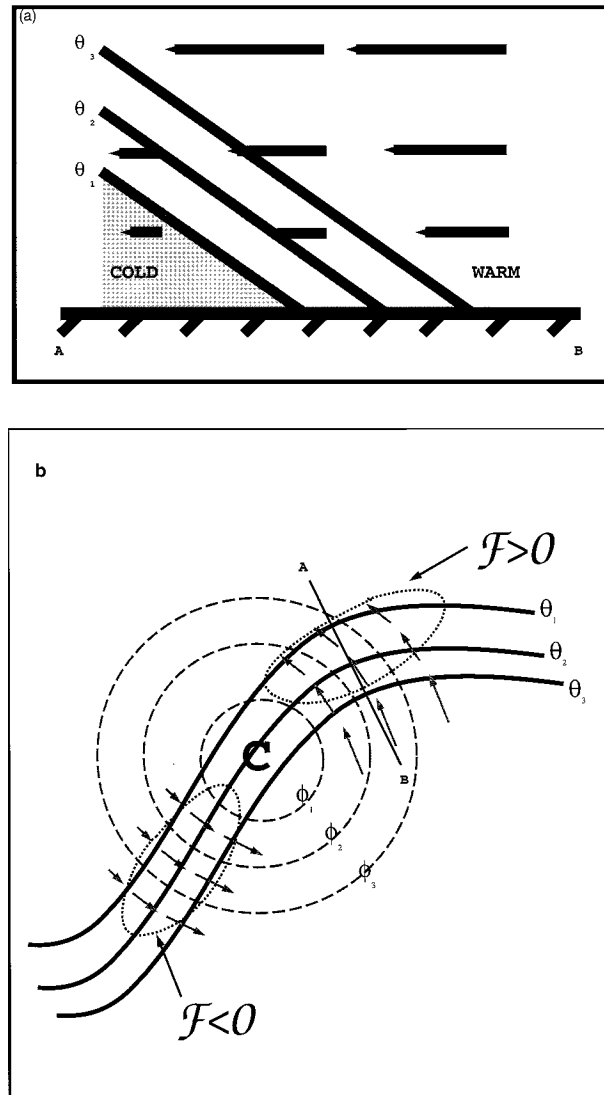


FIG. 22. Schematic of a positive upper-tropospheric PV anomaly interacting with lower-tropospheric baroclinic zone. (a) Schematic cross section (A-B) through a baroclinic zone: isentropes (solid, labeled $\theta_1, \theta_2, \theta_3$, with $\theta_1 < \theta_2 < \theta_3$) with winds (vectors) associated with upper trough; (b) horizontal map depicting lower-tropospheric isentropes (solid, dark contours), geopotential height perturbations associated with upper trough (gray contours; labeled $\varphi_1, \varphi_2, \varphi_3$, with $\varphi_1 < \varphi_2 < \varphi_3$), and geostrophic wind vectors (gray arrows) and associated frontogenesis regions enclosed with dotted contours. C indicates the center of the cyclonic circulation associated with the positive PV anomaly. Location of cross section (A-B) in (a) shown by heavy dashed line.

quency) is on average smallest. A baroclinic zone in a stably stratified atmosphere is characterized by isentropic surfaces sloping upward toward the coldest air (Fig. 22a). At a given level, the winds attributed to an upper-PV anomaly are weaker where the column-averaged N above that level is larger. If the winds associated with a large-scale upper-tropospheric PV anomaly were directed (as an example) from warm to cold, frontogenesis

would then be anticipated within the frontal zone. For winds directed from cold to warm, frontolysis would be anticipated. Figure 22b shows the configuration of lower-tropospheric isentropes and \mathbf{v}'_u in the lower troposphere for an upper trough overlaying a baroclinic zone.⁵ Frontogenesis (frontolysis) would be expected for flow directed from the cold (warm) side of the baroclinic zone to the warm (cold) side. We note that because the winds are nondivergent, this decrease in the magnitude of the wind normal to the isentropes must be accompanied with diffluence (characterized by a component of the wind parallel to the front).

There is some evidence for this effect occurring in the case presented: the front-normal component of \mathbf{v}'_u decreases as the flow is directed from warm to cold. Furthermore, frontogenesis had a propensity to occur along the northern portion of the thermal ridge where the flow was diffluent, while frontolysis occurred on the warm portion of the thermal ridge where the flow was confluent. The magnitude of the frontogenesis well exceeds the frontolysis—suggesting an asymmetry in the flow across the warm and cold sides of the baroclinic zone (Fig. 5c).

c. Extensions: Frontal dynamics

Surface and upper-tropospheric fronts are of meteorological significance as they are often associated with the development of mesoscale precipitation regions: the development and decay of fronts (frontogenesis and frontolysis, respectively) are associated with the front-normal ageostrophic Sawyer–Eliassen circulation, which, in the presence of sufficient moisture, may lead to cloudiness and precipitation. During the life cycles of midlatitude cyclones, the distribution and intensity of precipitation changes with time and these changes are, in part, related to processes associated with frontal dynamics or larger, cyclone-scale processes.

While the techniques and results presented in this study deal with the *kinematics* of frontogenesis they may be applied to the *dynamics* of frontogenesis as well. The dynamics of frontogenesis is widely understood as a two step process: geostrophic deformation facilitates both the initial intensification of the thermal gradient and the concomitant initiation of the Sawyer–Eliassen circulation, this circulation in turn has a positive feedback on the frontogenesis, accelerating the process to frontal collapse. In a local (n, s) coordinate system, the adiabatic, inviscid Sawyer–Eliassen circulation streamfunction (ψ^{SE}) is mathematically forced by the component of Q normal to the frontal zone, Q_n :

$$S \frac{\partial^2 \psi^{SE}}{\partial n^2} - 2B \frac{\partial^2 \psi^{SE}}{\partial n \partial p} + \zeta_a \frac{\partial^2 \psi^{SE}}{\partial p^2} = -Q_{gn}, \quad (6.1)$$

⁵ Note that in Fig. 18 the northward-flowing geostrophic winds are weaker in the cold air.

where the symbols S and B represent parameters proportional to the static stability and baroclinicity and ζ_a is the component of absolute vorticity normal to isobaric surfaces (Carlson 1991).

The ascending branch of the Sawyer–Eliassen circulation has been associated with banded precipitation structures along frontal zones undergoing frontogenesis. Having computed the partitioned pieces of the geostrophic \mathbf{Q} vector, one may determine the structure and intensity of the ageostrophic circulations associated with each piece. Due to the linearity of (6.1), ψ^{SE} may then be partitioned into parts associated with each of the forcing terms Q_{gn}^u , Q_{gn}^m , and Q_{gn}^l .

Acknowledgments. The author is grateful to Drs. John Nielsen-Gammon, Christopher Davis, Richard Rotunno, Jonathan Martin, and anonymous reviewers for comments on earlier versions of the manuscript. The author also thanks Dr. Davis for his providing the software used in inverting the PV. The work was supported in part by the National Science Foundation Grant ATM-9633418.

REFERENCES

- Black, R., and R. Dole, 1993: The dynamics of large scale cyclogenesis over the North Pacific Ocean. *J. Atmos. Sci.*, **50**, 421–442.
- Bresky, W. C., and S. J. Colucci, 1996: A forecast and analyzed cyclogenesis event diagnosed with potential vorticity. *Mon. Wea. Rev.*, **124**, 2227–2244.
- Carlson, T., 1991: *Midlatitude Weather Systems*. Routledge, 507 pp.
- Charney, J., 1955: The use of primitive equations of motion in numerical prediction. *Tellus*, **7**, 22–26.
- Davies, H., C. Schär, and H. Wernli, 1991: The palette of fronts and cyclones within a baroclinic wave development. *J. Atmos. Sci.*, **48**, 1666–1689.
- Davis, C. A., 1992a: Piecewise potential vorticity inversion. *J. Atmos. Sci.*, **49**, 1397–1411.
- , 1992b: A potential vorticity diagnosis of the importance of initial structure and condensational heating on observed extratropical cyclogenesis. *Mon. Wea. Rev.*, **120**, 2409–2428.
- , and K. Emanuel, 1991: Potential vorticity diagnostics of cyclogenesis. *Mon. Wea. Rev.*, **119**, 424–439.
- , M. T. Stoelinga, and Y.-H. Kuo, 1993: The integrated effect of condensation in numerical simulations of extratropical cyclogenesis. *Mon. Wea. Rev.*, **121**, 2309–2330.
- , E. D. Grell, and M. A. Shapiro, 1996: The balanced dynamical nature of a rapidly intensifying oceanic cyclone. *Mon. Wea. Rev.*, **124**, 3–26.
- Eliassen, A., and E. Kleinschmidt, 1957: Cyclones and anticyclones. *Dynamic Meteorology. Handbuch der Physik*, S. Flugge, Ed., Vol. 48, Springer-Verlag, 112–154.
- Gill, A., 1982: *Atmosphere–Ocean Dynamics*. Academic Press, 662 pp.
- Hakim, G., L. Bosart, and D. Keyser, 1996: The Ohio Valley wave-merger cyclogenesis event of 25–26 January 1978. Part II: Diagnosis using quasigeostrophic potential vorticity inversion. *Mon. Wea. Rev.*, **124**, 2176–2205.
- Holopainen, E., and J. Kaurola, 1991: Decomposing the atmospheric flow using potential vorticity framework. *J. Atmos. Sci.*, **48**, 2614–2625.
- Hoskins, B., 1976: Baroclinic waves and frontogenesis. Part I: Introduction and Eady waves. *Quart. J. Roy. Meteor. Soc.*, **102**, 103–122.
- , and N. West, 1979: Baroclinic waves and frontogenesis. Part

- II: Uniform potential vorticity jet flows—cold and warm fronts. *J. Atmos. Sci.*, **36**, 1663–1680.
- , and M. Pedder, 1980: The diagnosis of middle latitude synoptic development. *Quart. J. Roy. Meteor. Soc.*, **106**, 707–719.
- , I. Draghici, and H. Davies, 1978: A new look at the ω -equation. *Quart. J. Roy. Meteor. Soc.*, **104**, 31–38.
- , M. McIntyre, and A. Roberston, 1985: On the use and significance of isentropic potential vorticity maps. *Quart. J. Roy. Meteor. Soc.*, **111**, 877–946.
- , M. Reeder, and R. Reed, 1988: A generalization of Petterssen's frontogenesis function and its relation to the forcing of vertical motion. *Mon. Wea. Rev.*, **116**, 762–780.
- Keyser, D., B. Schmidt, and D. Duffy, 1992: Quasigeostrophic vertical motions diagnosed from along- and cross-isentropic components of the \mathbf{Q} Vector. *Mon. Wea. Rev.*, **120**, 731–741.
- Korner, S., 1998: Piecewise frontogenesis from a potential vorticity perspective: Methodology and a case study. M.S. Thesis, Department of Atmospheric and Oceanic Sciences, University of Wisconsin—Madison, 149 pp. [Available from Department of Atmospheric and Oceanic Sciences, Univ. of Wisconsin—Madison, 1225 W. Dayton St., Madison, WI 53706.]
- Martin, J., 1999: Quasi-geostrophic forcing for ascent in the occluded sector of cyclones and the trowal airstream. *Mon. Wea. Rev.*, **127**, 66–84.
- Miller, J., 1948: On the concept of frontogenesis. *J. Meteor.*, **5**, 169–171.
- Morgan, M. C., and J. Nielsen-Gammon, 1998: Using tropopause maps to diagnose midlatitude weather systems. *Mon. Wea. Rev.*, **126**, 2555–2579.
- Nielsen, J., C. Davis, and D. Keyser, 1991: Upper-level frontogenesis made easy? Preprints, *First Int. Symp. on Winter Storms*, New Orleans, LA, Amer. Meteor. Soc., 82–87.
- Nielsen-Gammon, J., and R. Lefevre, 1996: Piecewise tendency diagnosis of dynamical processes governing the development of an upper-tropospheric mobile trough. *J. Atmos. Sci.*, **53**, 3120–3142.
- Petterssen, S., 1936: Contribution to the theory of frontogenesis. *Geofys. Publ.*, **11**, 1–27.
- Ramos, R., 1997: The role of latent heat release on the development of an upper tropospheric outflow jet. M.S. Thesis, Department of Atmospheric and Oceanic Sciences Univ. of Wisconsin—Madison, 149 pp. [Available from Department of Atmospheric and Oceanic Sciences, Univ. of Wisconsin—Madison, 1225 W. Dayton St., Madison, WI 53706.]
- Rotunno, R., W. C. Skamarock, and C. Snyder, 1994: An analysis of frontogenesis in numerical simulations of baroclinic waves. *J. Atmos. Sci.*, **51**, 3373–3398.
- Sanders, F., and B. Hoskins, 1990: An easy method for estimation of \mathbf{Q} -vectors from weather maps. *Wea. Forecasting*, **5**, 346–353.
- Schultz, D. M., D. Keyser, and L. Bosart, 1998: The effect of large-scale flow on low-level frontal structure and evolution in mid-latitude cyclones. *Mon. Wea. Rev.*, **126**, 1767–1791.
- Shapiro, M., and D. Keyser, 1990: Fronts, jet streams, and the tropopause. *Extratropical Cyclones. The Erik Palmén Memorial Volume*, C. Newton and E. Holopainen, Eds., American Meteorological Society, 167–191.